Bioactive Materials 7 (2022) 426–440

Contents lists available at ScienceDirect

Bioactive Materials

journal homepage: www.sciencedirect.com/journal/bioactive-materials

Biodegradation behaviour of Fe-based alloys in Hanks' Balanced Salt Solutions: Part I. material characterisation and corrosion testing

Christabelle Tonna [a,*], Cheng Wang [b], Di Mei [b,c], Sviatlana V. Lamaka [b], Mikhail L. Zheludkevich [b,d], Joseph Buhagiar [a]

[a] Department of Metallurgy and Materials Engineering, University of Malta, Msida, Malta
[b] Institute of Surface Science, Helmholtz-Zentrum Hereon, Geesthacht, 21502, Germany
[c] School of Materials Science and Engineering & Henan Key Laboratory of Advanced Magnesium Alloy, Zhengzhou University, Zhengzhou, 450001, PR China
[d] Institute for Materials Science, Faculty of Engineering, Kiel University, Kiel, 24103, Germany

ARTICLE INFO

Keywords:
Fe alloys
Biodegradable metals
Powder metallurgy
Electrochemical impedance spectroscopy
Local pH
Local DO

ABSTRACT

Research on Fe-based biodegradable alloys for implant applications has increased considerably over the past decade. However, there is limited information on the influence of testing electrolytes on corrosion product formation and general corrosion progress. In this work, the effect of Hanks' Balanced Salt Solution (HBSS) with or without Ca^{2+} on the corrosion of Fe, Fe35Mn and (Fe35Mn)5Ag powder-processed coupons has been studied using potentiodynamic polarisation, Electrochemical Impedance Spectroscopy (EIS), and preliminary localised measurement of pH and dissolved oxygen concentration in close proximity to the metal surface. Both Fe35Mn and (Fe35Mn)5Ag alloys showed accelerated corrosion when compared to pure Fe based on potentiodynamic testing results, with FeMnAg exhibiting the highest corrosion rate in Ca^{2+}-containing HBSS. The results indicate that in Ca^{2+}-containing HBSS, the formation of a partially protective Ca/P layer decelerates the corrosion progress, whereas the Fe- and Mn-phosphates formed in Ca^{2+}-free HBSS do not have the same effect. The Ca/P layer on (Fe35Mn)5Ag experienced a reduction in resistance following several hours of testing, indicating partial loss of its protective effect.

1. Introduction

Research on the development of new and improved biodegradable metallic implants has been on the rise for the past decade, especially with such implants reaching the market in recent years [1]. Magnesium and its alloys have by far been the most studied metals for such applications, however various studies have shown that for some applications the corrosion rate of selected magnesium alloys is higher than optimal [2]. The use of Fe as a biodegradable metal was first proposed by Peuster et al. [3] who, following *in vivo* testing, suggested that alloying and surface modification must be employed to enhance the inadequately slow degradation of pure Fe. Zinc alloys have also shown the potential to provide optimal balance between Mg- and Fe-alloys in terms of their degradation rate performance, however the main limitation of Zn lies in its low strength and limited plasticity [4]. One must keep in mind that the ideal degradation rate and mechanical properties vary depending on the implantation region and specific clinical case. Literature suggests that for cardiovascular stents, complete degradation should progress following vessel remodelling which should take around four months, while bone implants should maintain their structural integrity for 12–24 months before completely degrading [5].

The development of Fe-alloys to approach the desired performance, has benefitted from major contributions by Hermawan et al. [6] in a series of initial studies investigating the influence of Mn as a significant alloying element [6–10]. Encouraging indications of accelerated degradation were obtained from early potentiodynamic polarisation tests carried out on sintered and cold-rolled Fe35Mn, supplementing an antiferromagnetic austenitic structure that is better suited for implant applications [7]. Further improvements were introduced and developed by Schinhammer et al. [11] with proposed ternary alloys of FeMn-X, where

Peer review under responsibility of KeAi Communications Co., Ltd.
* Corresponding author.
E-mail address: christabelle.tonna@um.edu.mt (C. Tonna).

https://doi.org/10.1016/j.bioactmat.2021.05.048
Received 14 November 2020; Received in revised form 19 April 2021; Accepted 26 May 2021
Available online 20 June 2021

X is a noble element such as Pd, that leads to an immiscible, more noble phase within the base FeMn matrix, to trigger enhanced micro-galvanic corrosion [11–14]. In such cases, microsites in the material with higher potentials than the base metal, behave as local cathodes, accelerating the anodic dissolution of the less noble phase.

Potentiodynamic polarisation and immersion tests are often employed to obtain indicative corrosion rates for materials of interest. Potentiodynamic polarisation tests allow for a relatively fast approach towards assessing the material's immediate condition through measurement of corrosion current while static immersion tests allow for monitoring of corrosion rates through weight-loss measurements over a relatively long period of time. Published immersion tests on pure Fe all point towards uniform corrosion as the dominant corrosion mechanism *in vitro*, with Moravej et al. [15] recording a corrosion rate of 0.25 ± 0.02 mm/year in Hanks' Balanced Salt Solution (HBSS) [15–18]. Small additions of Mn (up to 6.9 wt.%), seem to make little effect on the degradation rate [19,20]. On the other hand, various publications studying additions of 20–35 wt.% Mn have reported accelerated degradation rates [21–24], with Dehestani et al. [22] observing ten times the corrosion rate of pure Fe when testing Fe30Mn in Kokubo's solution. In these cases, the authors typically attribute the increase in degradation partly to micro-galvanic corrosion due to elemental inhomogeneity in the distribution of Mn. Hermawan et al. [8] noted that the degradation increased with decreasing Mn content, due to the presence of a bi-phasic microstructure at concentrations of 20 and 25 wt.% Mn. However, the presence of micro-galvanic corrosion, does not mean that corrosion occurred in a localised manner, as Hermawan et al. [7] also referred to the uniform corrosion observed on the FeMn alloys.

Ternary alloys of FeMn with a noble element addition were specifically suggested to drastically increase the effect of micro-galvanic corrosion. The proposed strategy seemed to be successful when Pd was added to FeMnC steel, with static immersion tests repeatedly showing increased corrosion rates [11,12]. The addition of Ag to FeMn was also successful in a study by Sotoudeh Bagha et al. [25] where just 1 wt.% Ag addition to Fe30Mn led to doubling of the corrosion rate in HBSS. Contrarily, in a recent study by Loffredo et al. [26], the addition of 0.4 wt.% Ag to Fe16Mn0.7C, decreased the corrosion rate.

Naturally, the compositional changes are not the only contributing factors to variation in corrosion rates and behaviour. With powder metallurgy processing being one of the most employed routes in the preparation of test samples and potential implants, various researchers have studied and confirmed the positive effect of increasing the amount of porosity, has on achieving a higher degradation rate [21,22,27]. Others also noted the effect of increasing residual stresses and internal defects on the increase of degradation [28–30]. Apart from material-related variables, changes in the electrolyte and testing setups have drastic effects on test outcomes. Tests carried out under a flow of electrolyte tend to result in higher recorded corrosion rates, due to the flushing of corroding areas from loose products that are obstructing the bare metal [15,31]. Addition of protein to HBSS seems to result in lower corrosion rates due to the biofilm that forms at the surface [32,33]. Mouzou et al. [34] showed that Fe20Mn1C exhibited a higher corrosion rate of 0.165 mm/year in Ca^{2+}-free HBSS as opposed to modified HBSS (containing Ca^{2+}) where the corrosion rate was 0.115 mm/year.

The above closely relates to the corrosion products observed on immersion tested metals. Multiple studies indicate that the corrosion products on Fe-based alloys, form a two-layer structure of reddish-brown product (Fe_2O_3) on a dark product (Fe_3O_4) in contact with substrate [8]. Indeed, reddish-brown products are often observed, even in *in vivo* studies. Despite the fact that there was no significant reduction in coupon volume in an *in vivo* study carried out by Kraus et al. [35] when Fe–21Mn-0.7C–1Pd pins were immersed in the femur of Sprague–Dawley rats for 52 weeks, optical images clearly show the reddish-brown products mentioned in *in vitro* studies. Similar observations were made in two other *in vitro* studies with FeMn alloys [19,36]. Additionally, reference is often made to the formation of Ca/P products at the surface. Sing et al. [30] mention that precipitation of Ca/P products on Fe35Mn stent samples immersed in Simulated Body Fluid (SBF) started around 30 min after immersion. Zhang et al. [17] detected $Fe_3(PO_4)_2{\cdot}8H_2O$ and $Ca_3(PO_4)_2$ on the surface of Fe coupons immersed in HBSS using XRD, however the specific formulation of HBSS was not specified. Varying degrees of precipitation of $MnCO_3$ was detected on the surface after 14 days of immersion in a study by Mouzou et al. [34] depending on the amount of carbonates present in the testing electrolyte. The precipitation of these carbonates in carbonate-rich electrolyte is suggested to have increased the local pH to stimulate further phosphate/carbonate deposition. The extent to which such products have been reported to retard corrosion, has varied significantly. All this points towards strong dependencies of corrosion product formation on the electrolyte formulation, consequent product solubility and their effect on the local precipitation environment [34,37–39].

Electrochemical Impedance Spectroscopy (EIS) is another useful means of observing changing characteristics of key components and features of the corroding system. Recent studies have made use of this technique to better understand the corrosion of Fe-based alloys upon immersion. Over a typical frequency range (0.1–10^5 Hz), a time constant at low frequencies, is generally present to represent the metal's charge-transfer behaviour at the metal-electrolyte interface. However, a time constant at higher frequencies has been observed in several studies that could be attributed to the formation of partially protective corrosion layers and products on the corroding metal surface [40,41]. In general, it has been shown that pure Fe tends to display one time constant as opposed to the two-time constant systems exhibited by FeMn alloys, indicating the latter's ability to develop protective layers of corrosion products soon after immersion [21,28]. FeMn also has a tendency to have lower polarisation resistances compared to Fe, indicating lower corrosion resistance [21,23]. Similarly, the addition of Pd [11] and Ag [25] led to lower polarisation resistances compared to their FeMn counterparts. In an interesting study by Schinhammer et al. [13], EIS was conducted at intervals on Fe21Mn0.7C1Pd immersed in SBF for several hours, showing a clear formation of the time constant at higher frequencies. A similar study by Wiesener et al. [40] showed the same effect on SLM-processed Fe22Mn5Ag immersed in SBF for 38 h, indicating the steady growth of corrosion products over the period of study. These observations highlight similarities between corroding Mg and Fe-alloys in corrosion product formation influenced by electrolyte formulation, as the same effect was also reported in recent studies on biodegradable Mg in similar Ca^{2+}-containing SBF-like electrolytes [41,42].

In this work, EIS and potentiodynamic polarisation tests are used to evaluate the effect of Mn and Ag addition to pure Fe through the study of powder-processed Fe, Fe35Mn and (Fe35Mn)5Ag. Testing was carried out in two different formulations of HBSS (with and without Ca^{2+} ions) followed by observations of resulting product formation in the first 24 h from immersion. Moreover, work on the monitoring of local interface pH and dissolved oxygen (DO) levels is briefly shown here and is discussed in more depth in Part II of this work [43]. The importance of localised environment measurements arises from the fact that the principal degradation reactions of Fe-based alloys in typically used corrosion testing media in the field, could be described by the anodic reaction (reaction **1**) and the corresponding cathodic reaction involving the reduction of oxygen (reaction **2**).

$$Fe \rightarrow Fe^{2+} + 2e^- \quad (1)$$

$$O_2 + 4e^- + 2H_2O \rightarrow 4OH^- \quad (2)$$

The monitoring of DO levels could therefore provide insight into the progression of the cathodic reaction, whereas the local pH could also provide complementary information. However, the latter is also affected by the acidification of the electrolyte as a result of hydrolysis reactions

(reactions **3** and **4**) [44] and therefore gives information about the combined effect of multiple corrosion reactions.

$$Fe^{2+} + 2H_2O \rightarrow Fe(OH)_2 + 2H^+ \quad (3)$$

$$Fe^{3+} + 3H_2O \rightarrow Fe(OH)_3 + 3H^+ \quad (4)$$

2. Materials and methods

2.1. Material preparation

The materials investigated in this study were Fe, Fe35Mn and (Fe35Mn)5Ag, subsequently referred to as Fe, FeMn and FeMnAg respectively. The alloys were produced using raw elemental powders: Fe (particle size <45 μm, 99% purity, US Research Nanomaterials Inc. USA), Mn (particle size <10 μm, 99.6% purity, Alfa Aesar, Germany) and Ag (particle size 4–7 μm, 99.9% purity, Alfa Aesar, Germany). The powders were placed in a 50 ml centrifuge tube in the ratio specified above and mixed in a Bio-Components Inversina tumbler (Switzerland) for 5 h with 10 mm diameter stainless steel balls, to homogenise the powder mixture. In the case of (Fe35Mn)5Ag, the amounts of Fe and Mn were adjusted to have a 65:35 Fe to Mn ratio.

For EIS and potentiodynamic measurements, a charge of 10 g powder from each mix was loaded in a uniaxial press having a die 22 mm in diameter and pressed at 520 MPa using an Instron 8802 hydraulic press (USA). The samples for local pH and dissolved oxygen (DO) measurements were prepared by pressing 6 g of the same powder mixtures in an 8 mm die using a pressure of 1.8 GPa. The compacts were placed in a tube furnace (Nabertherm, Germany) and sintered for 3 h at 1120 °C following a heating rate of 180 °C/h under a 100 L/h flow of N_2–$5H_2$ gas. Following sintering, the heating element was switched off and the samples were allowed to furnace cool. In each case, the sintered coupons were ground to remove the Mn oxide-rich outer layer that forms due to high temperature oxidation of Mn. For local pH and DO measurements, the samples were turned using a machine lathe to produce pins, 3 mm in diameter. All samples were mounted in epoxy resin and ground to P2500 using SiC paper (Metprep, UK). Samples were polished using 3 μm diamond suspension (Struers, Denmark) and finally by 0.04 μm colloidal silica (Struers, Denmark) for initial SEM analysis. Cleaning included ultrasonication in acetone and ethanol for 5 min each, followed by air and vacuum drying. Prepared samples were stored in a desiccator until use.

2.2. Characterisation

Microstructural and EDS analysis was carried out using a Carl Zeiss FE-SEM Merlin Gemini II column (Germany) equipped with an Ametek EDAX energy dispersive X-ray detector (USA). The working voltage was set at 15 kV while the probe current was set to 3 nA. An estimation of the sample porosity was calculated by measuring the percentage porous area. For each material, 30 SEM images from three separate samples were binarised and analised using ImageJ software. Phase analysis was carried out using a Bruker D8 Advance (USA) X-Ray Diffractometer with a copper source (Cu-Kα, λ = 0.141 nm) and equipped with a graphite monochromator. All samples were analysed at 2θ angles between 30° and 100°, with the step size set to 0.02°. The diffractometer was set to move at 1°/min while sample rotation was set to 15°/min. Diffraction patterns were analysed using PDXL software.

2.3. Potentiodynamic polarisation tests

Potentiodynamic polarisation (PDP) tests were carried out in 300 ml of two different electrolytes open to air: Ca^{2+}-free HBSS (ThermoFisher Scientific, no. 14175095) hereafter denoted as HBSS and Ca^{2+}-containing HBSS (ThermoFisher Scientific, no. 14025100), containing 1.26 mM $CaCl_2$, 0.49 mM $MgCl_2{\cdot}6H_2O$ and 0.41 mM $MgSO_4{\cdot}7H_2O$ along with other HBSS components, hereafter denoted as HBSS+Ca. The complete formulation of both electrolytes is listed in Table 1. Tests were done at 37 ± 2 °C from −250 mV to +250 mV vs. OCP, after the system was allowed to stabilise considerably for 1 h. The scanning rate was set to 0.5 mV/s to prevent significant shifting of the OCP due to a slower scanning rate. Tests were carried out using a three-electrode setup consisting of a Gamry Interface 1000 potentiostat (USA), a platinum counter electrode and a Saturated Calomel Electrode (SCE) as a reference. The apparent area exposed to the electrolyte was that of 1 cm^2. Measurements were repeated four times on different samples and corrosion current densities were calculated using Tafel extrapolation.

Table 1
The formulation of HBSS and HBSS+Ca electrolytes used in this study.

Components	HBSS (mM)	HBSS+Ca (mM)
KCl	5.333	5.333
KH_2PO_4	0.441	0.441
$NaHCO_3$	4.167	4.167
NaCl	137.9	137.9
Na_2HPO_4	0.338	0.338
$CaCl_2$	–	1.261
$MgCl_2{\cdot}6H_2O$	–	0.493
$MgSO_4{\cdot}7H_2O$	–	0.407
D-Glucose	5.556	5.556

2.4. Electrochemical Impedance Spectroscopy

EIS tests were performed on each material in 400 ml of HBSS or HBSS+Ca at 37 ± 2 °C over a period of 24 h using the three-electrode setup described for the potentiodynamic polarisation tests. The frequency range investigated was from 100 kHz to 0.1 Hz with 10 points/decade at an AC voltage of 10 mV rms from OCP. Measurements at lower frequencies were avoided to prevent polarisation of the sample surface. The apparent area exposed to the electrolyte was 1 cm^2 as for the potentiodynamic polarisation tests. Tests were repeated three times to ensure similar behavioural trends. Following EIS tests, the samples were rinsed well in de-ionised water and vacuum dried. Corrosion products adherent to the surface could then be analysed using SEM and EDS analysis. Fitting of the impedance spectra was carried out using EChem Analyst (Gamry, USA).

2.5. Local pH and dissolved oxygen monitoring

To gain insight into the local changes in pH and dissolved oxygen concentration (DO) upon immersion of the metal in the electrolyte, simultaneous measurement of pH and DO at the centre of each coupon, were recorded 50 μm above the sample surface, as shown schematically in Fig. 1. For DO measurement, a needle-type retractable fibre-optic oxygen micro-optode with a diameter of 50 μm coupled with FireStingO2 oxygen logging meter (Pyroscience™, Germany), were used. The pH was measured by a glass-type pH microelectrode with the tip length of 50 μm and tip diameter of 10 μm (Unisense, Denmark). The pH

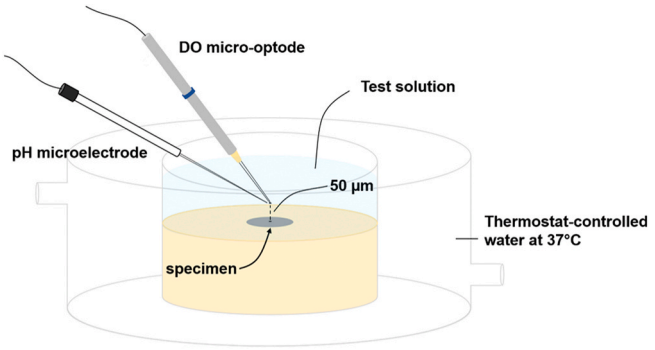

Fig. 1. Schematic of setup for local pH and DO measurement.

microelectrode was immobilized at 50 μm above the sample surface together with the DO micro-optode using 3D motorized positioning system making part of SVET equipment (Applicable Electronics and Sciencewares, USA). The distance between pH microelectrode and DO micro-optode was controlled using a dual-head stage micromanipulator and kept at 50 μm in horizontal planes. The total volume of electrolyte in the flow-through measurement cell was 4 ± 1 ml with the solution surface reaching a height of around 5 mm above the specimen surface. The temperature of the electrolyte was kept at 37 ± 1 °C using thermostat-controlled water flowing through a custom-made water-jacket. Prior to test initiation, the DO concentration in the electrolytes saturated with air, was measured at 5.8 ± 0.2 mg/L. A more comprehensive description of local pH and DO measurements is presented in Refs. [45, 46] and in Part II of this work [43].

3. Results

3.1. Material characterisation

The microstructures of the prepared alloys, as analysed using SEM, are shown in Fig. 2. The images showing the microstructure of Fe (Fig. 2 a-b), clearly show a single phase with a relatively low amount of porosity (8.58 ± 0.52%) compared to the structure of the FeMn-alloys (19.04 ± 1.27% and 18.45 ± 1.47% for FeMn and FeMnAg respectively). The higher amount of porosity observed in the latter may be attributed to the decrease in compressibility of the powder mixture during the preparation of the green coupons due to the addition of the harder Mn raw material [47]. The FeMn microstructure (Fig. 2 c-d) also shows the presence of a single phase matrix, however it also includes O-rich inclusions, as shown in the EDS maps in Fig. 3 for both the FeMn and FeMnAg microstructures. The presence of oxygen in the pore suggests that manganese oxide is also present in the open pores. EDS analysis of areas (**1**) and (**2**) in Fig. 2d,f also confirms that the weight ratio of Fe:Mn in the material matrix is within the expected ratio. The slightly lower amount of Mn than the 35 wt% added, could be due to losses from oxidation and slight elemental inhomogeneities in the austenitic phase. The homogeneous dispersion of the lighter phase in the FeMnAg microstructural images (Fig. 2e–f), corresponds to the immiscible Ag, as better exhibited in the elemental distribution maps in Fig. 3. The addition of Ag allows for liquid-phase sintering to take place at temperatures higher than 962 °C, at which point this metal melts.

The XRD patterns observed in Fig. 4 confirm the sole presence of the ferritic phase (α-Fe, PDF Card No. 04-015-2437) in the Fe microstructure, while the successful diffusion of Mn into Fe in the FeMn and FeMnAg microstructures is evidenced by the presence of the high intensity austenitic reflections (γ-FeMn, PDF Card No. 04-006-6664) and no visible residuals of the raw α-Fe and α-Mn phase. The O-rich phase observed in Fig. 2d, f is confirmed by XRD to be MnO (PDF Card No. 04-002-8159), a result of the high affinity of Mn to oxygen in the sintering conditions [48] and is present in both Fe35Mn and (Fe35Mn)5Ag structures. The latter also showed evidence of the Ag-rich phase (PDF Card No. 01-080-4432) in the microstructure. This oxide could also have contributed to limited diffusion at the sintering temperatures, thus preventing further densification of the FeMn and FeMnAg alloys.

3.2. Potentiodynamic polarisation

Tafel plots obtained from PDP testing of the alloys, are presented in Fig. 5a, while corresponding calculated corrosion current densities (i_{corr}) are shown in Fig. 5b. Despite the rather large error range displayed for the FeMnAg alloy, measurements of i_{corr} for the metals indicate that corrosion is generally faster in HBSS compared to HBSS+Ca. In HBSS+Ca, FeMnAg clearly exhibits a higher current density than FeMn, which in turn corroded faster than Fe. Both FeMn and FeMnAg also had higher i_{corr} values compared to Fe in HBSS. One must note that the corrosion current densities may be slightly overestimated due to the porous nature of the working electrodes used.

3.3. Electrochemical Impedance Spectroscopy

EIS was used to characterise the corrosion behaviour of the Fe-based alloys, arising both from the change in testing medium as well as from the alloy composition. Representative Bode plots, shown in Fig. 6, illustrate the change in impedance and phase shift as a function of frequency over a 24-h testing period, for coupons exposed to HBSS and HBSS+Ca.

In general, the most apparent difference between the two sets of data, is the additional distinct time constant observed in all tests carried out in HBSS+Ca. In HBSS, the samples only exhibited a single time constant at frequencies around which the double layer capacitance and charge transfer resistance of Fe-based alloys generally respond [13,21,

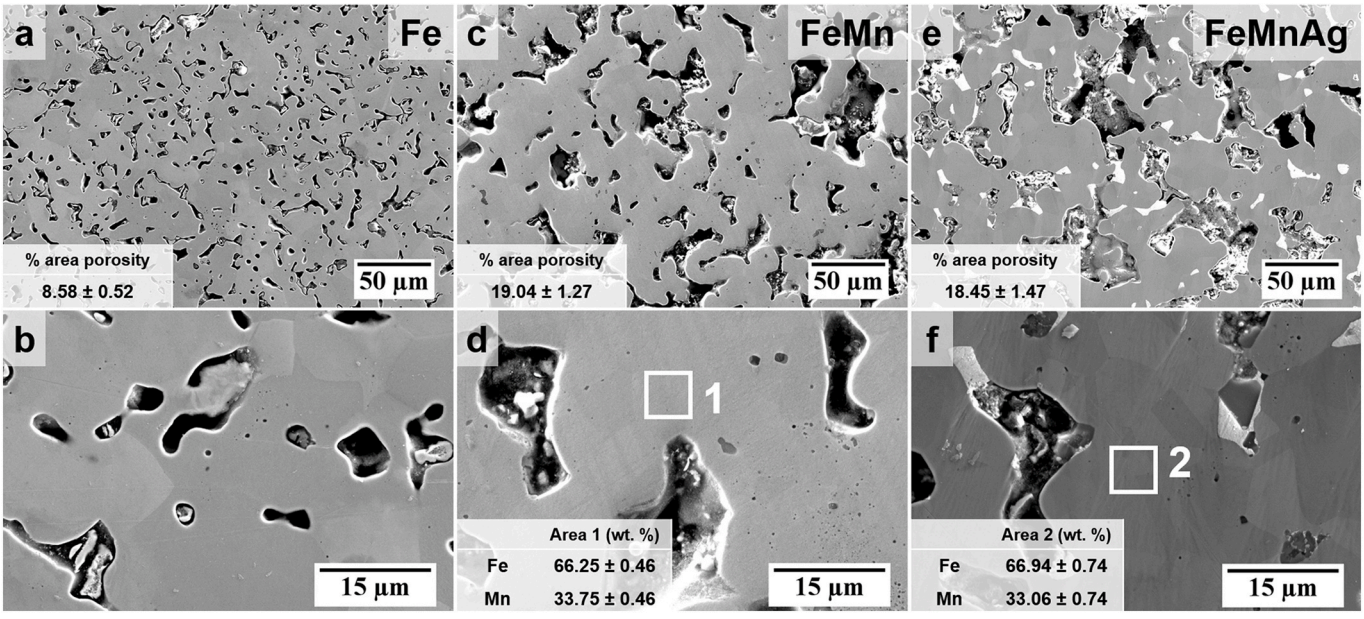

Fig. 2. SEM images of the ground and polished Fe (a–b), FeMn (c–d) and FeMnAg samples. (a), (c) and (e) include measurements of % porous area in the microstructures while (d) and (f) include the Fe:Mn ratios of the austenitic regions in the microstructure with standard errors (n = 30).

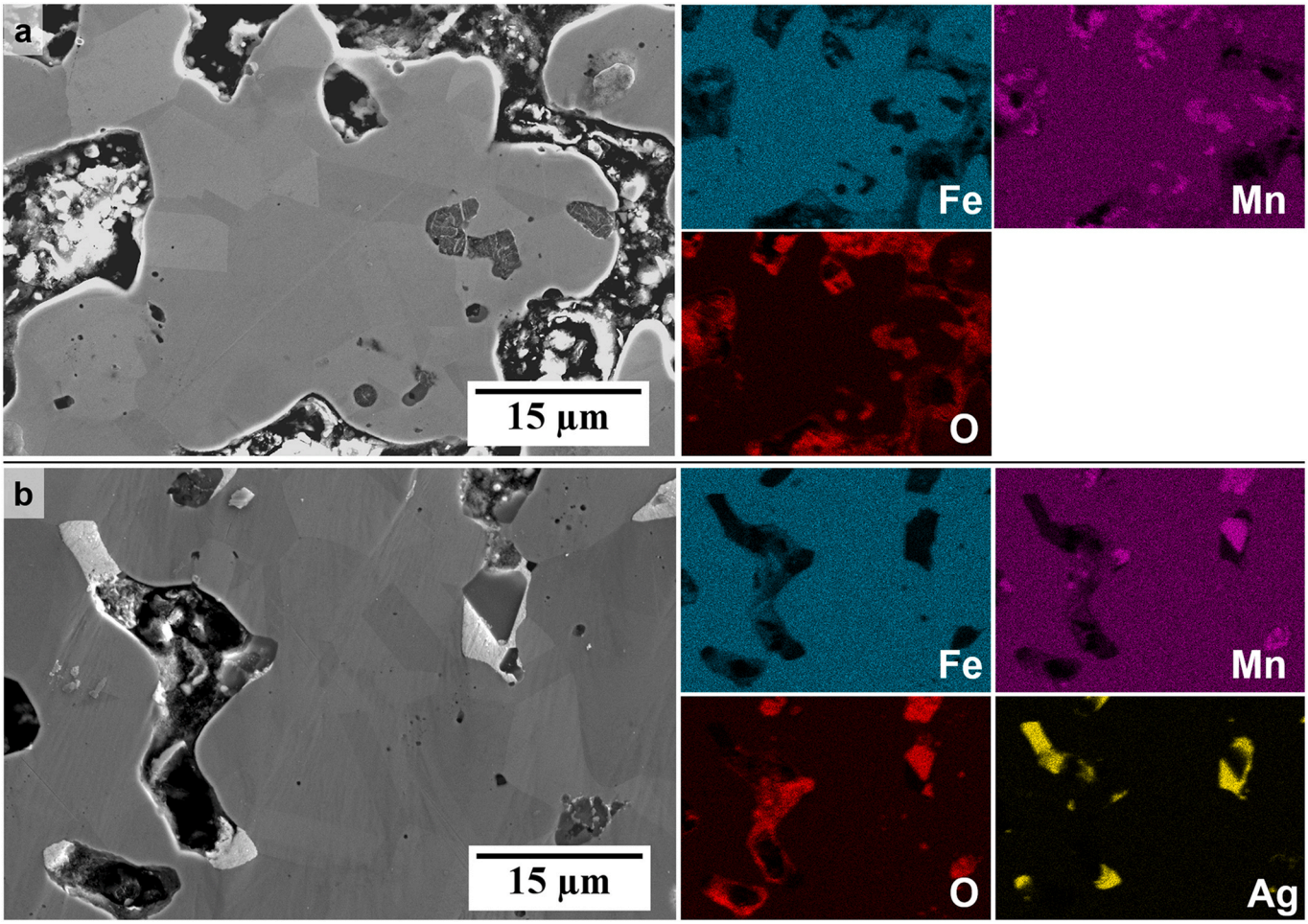

Fig. 3. EDS distribution of (a) Fe, Mn and O for the FeMn microstructure and (b) Fe, Mn, Ag and O for the FeMnAg microstructure.

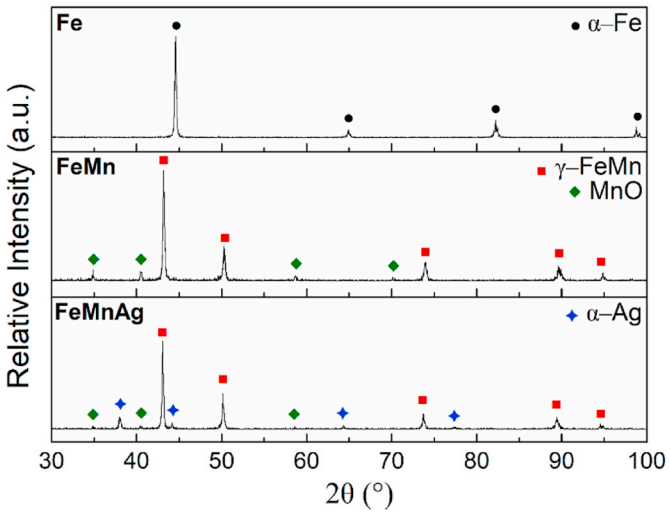

Fig. 4. XRD patterns for Fe, FeMn and FeMnAg material surface.

40]. On the other hand, the alloys in HBSS+Ca displayed another time constant formed at middle frequencies. In the case of pure Fe, the mid-frequency time constant was not obviously visible after the first 30 min of immersion. However, compared to the phase shift of Fe tested in HBSS at the same time, there is an obvious departure from the approximate 0° shift exhibited by the latter. The additional time constant could be attributed to a partially protective corrosion product layer. In the case of FeMn and FeMnAg, the additional time constant was evident from the initial run and progressed similarly over the following hours, with an increase in phase shift accompanied by an increase in mid-frequency impedance. After approximately 9 h, the mid-frequency time constant exhibited a decreasing negative phase shift accompanied by a decrease in mid-frequency impedance for FeMnAg. For better understanding of the corrosion layer evolution, the spectra for the alloys immersed in HBSS+Ca were fitted using the equivalent circuit shown in Fig. 7b. R_{el} corresponds to the electrolyte resistance while R_{ct} and CPE_{dl} represent the charge transfer resistance and double layer capacitance respectively. R_{layer} corresponds to the resistance of the additional protective layer whereas CPE_{layer} represents its capacitive behaviour. Constant phase elements were used instead of capacitors to account for the nonideal behaviour of features in realistic systems. The full results of the fitting may be found in the **Supplementary Material** for this manuscript. The value of true capacitance of the additional layer, C_{layer}, could then be calculated from the fitted values [49]. The evolution of R_{layer} and C_{layer} over the 24 h period is shown in Fig. 7c–d. In general, the growth of the resistance of the additional layer (R_{layer}) for Fe in HBSS+Ca, gradually increased over the 24 h period. In the case of FeMn, the R_{layer} value exhibited a steeper increase upon immersion followed by a gradual increase over the course of the test. On the other hand, while the R_{layer} for FeMnAg showed an even steeper increase upon immersion, the resistance started to drop after around 9 h, corresponding to the changes observed in the Bode plot. A similar trend can be observed in the evolution of C_{layer} where the values increased suddenly for FeMnAg after around 11 h. The capacitance of the layer on the FeMnAg alloy gradually

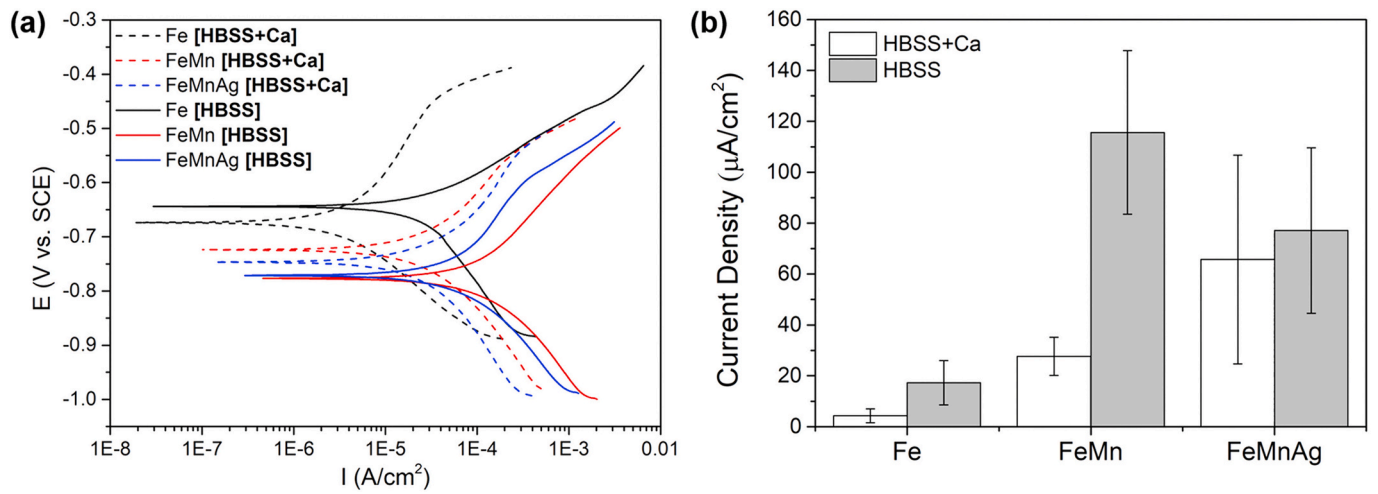

Fig. 5. (a) Tafel curves for Fe, FeMn and FeMnAg tested in HBSS and HBSS+Ca and (b) corresponding corrosion current densities for tested alloys. Error bars represent standard deviation (n = 4).

decreased again towards the original values. Since the capacitance has an inverse correlation with impedance, the sudden increase observed indicates a decrease in impedance contribution from the additional protective layer.

In the tests carried out in HBSS, one could clearly observe that the FeMn and FeMnAg had a much lower initial low frequency impedance compared to pure Fe. Over the course of the test, the low frequency impedance of FeMn and FeMnAg increased considerably while that for Fe decreased with time. In general, these trends were also observed in the tests conducted in HBSS+Ca, with the exception of pure Fe, which started off with a comparably high low-frequency impedance and retained generally high impedances for 24 h in HBSS+Ca. The development of low-frequency impedance in both electrolytes is better illustrated in Fig. 7a. Also observed at low frequencies in the tests done on FeMn and FeMnAg, is an additional relaxation process which could be attributed to diffusion limitations primarily due to the more porous nature of the FeMn and FeMnAg samples. Sharma et al. [50] observed this behaviour at similar frequencies when testing microporous Fe samples whereas the behaviour of denser samples corresponded to the spectra observed in this work for Fe in HBSS. This behaviour can also be observed in the Nyquist plots presented in the **Supplementary Material**. Due to the difficulty in achieving an adequate fit of diffusion through complex irregular pore geometries [51,52] as well as limitations of modelling low frequency measurements for actively degrading materials [13], the fitting results presented for the alloys in HBSS+Ca, excluded the low frequency ranges where the diffusion behaviour was observed. It is also interesting to note that in general, the impedance measured at 0.1 Hz in HBSS+Ca was considerably higher than that observed in Ca^{2+}-free HBSS. Mei et al. [41] also observed this when analysing the role of individual components of SBF on the corrosion of commercially pure Mg. In that study, SBF containing a combination of Ca^{2+}, HPO_4^{2-} and HCO_3^- also led to significantly higher low frequency impedances when compared to the same material tested in simple SBF without the trio of ions.

3.4. Corrosion product characterisation

The SEM-EDS images in Fig. 8 and Fig. 9 show the composition and morphology of corrosion products formed on Fe after EIS testing for 24 h in HBSS and HBSS+Ca, respectively. As can be seen in the SEM micrographs, both Fe samples exhibited a 'flaky' corrosion product layer. This characteristic of the layer could be due to post-experiment dehydration, as suggested by Schinhammer et al. [13]. In Fig. 9a–b, it is evident that the product layer seems denser in certain areas. Table 2, which contains EDS results for analysis on regions of interest on the corroded surfaces, shows values corresponding to spot and area analysis on Fig. 8a (point **1**) and Fig. 9b (area **2**). The results confirm that the product was an Fe/P-rich compound with similar at.% ratios on both test specimens. For the sample immersed in HBSS+Ca, however, there was also a distribution of bright white products. EDS mapping showed the presence of Ca in corresponding regions. In Fig. 9b it is also evident that the Fe/P layer is most likely loosely bound, as part of the layer was dislodged during the sample preparation process for microscopic analysis, revealing a pit in the Fe substrate. Moreover, Fig. 9a also shows that the Fe/P layer is also present in regions where the SiC paper scratches from the sample preparation process were still visible and an obvious scale was not apparent. The particle present in this image consisted of Na, Cl and C indicating that it is not likely a degradation product.

In the case of FeMn tested in HBSS, Fig. 10a–b did not show an obvious growth of a similar 'flaky' product. However, phosphate-rich deposits could be seen dispersed all over the sample surface and inside shallow pores (points **4** and **5**). For the FeMn sample tested in HBSS+Ca, Fig. 10c similarly indicates that there were no significant areas of 'flaky' product formation. However, one could observe localised growth of Ca/P-rich products (point **6**), beneath which lay a cracked layer that was richer in Fe and Mn (point **7**).

The morphology and composition of the FeMnAg surfaces after testing in both electrolytes were quite similar to those of the FeMn products, as shown in Fig. 11 and Fig. 12 and confirmed in corresponding EDS analysis. On the sample tested in HBSS, the maps showed the absence of the 'flaky' layer and a dispersion of phosphate-rich deposits including concentrated flower-like Mn/P-rich corrosion products (point **9**), as observed on the FeMn surface (point **5**). Such deposits are likely to be Mn-phosphates based on corresponding EDS maps and point analyses. Fe/Mn/P-rich deposits were also confirmed to be present in shallow pores based on EDS maps and spot analysis (point **10**). Ca/P products on a cracked corrosion product layer were likewise seen for FeMnAg tested in HBSS+Ca and EDS analysis confirmed similar trends in product composition. EDS maps also suggest that pores contained higher concentrations of the Ca/P-rich precipitates compared to the larger bare metal areas as indicated by red arrows on Fig. 12 and corresponding white arrows on the Ca/P/O maps.

Interestingly, EDS analysis on spots on the bare, seemingly non-corroded surfaces, where the scratches from the sample preparation process were still visible (Fig. 10, spots **3** and **8**), registered a higher O at.% compared to a similar area analysed prior to corrosion testing. This may indicate that although not obviously visible, a very thin layer of metal oxides/hydroxides could also be present in certain areas. In fact,

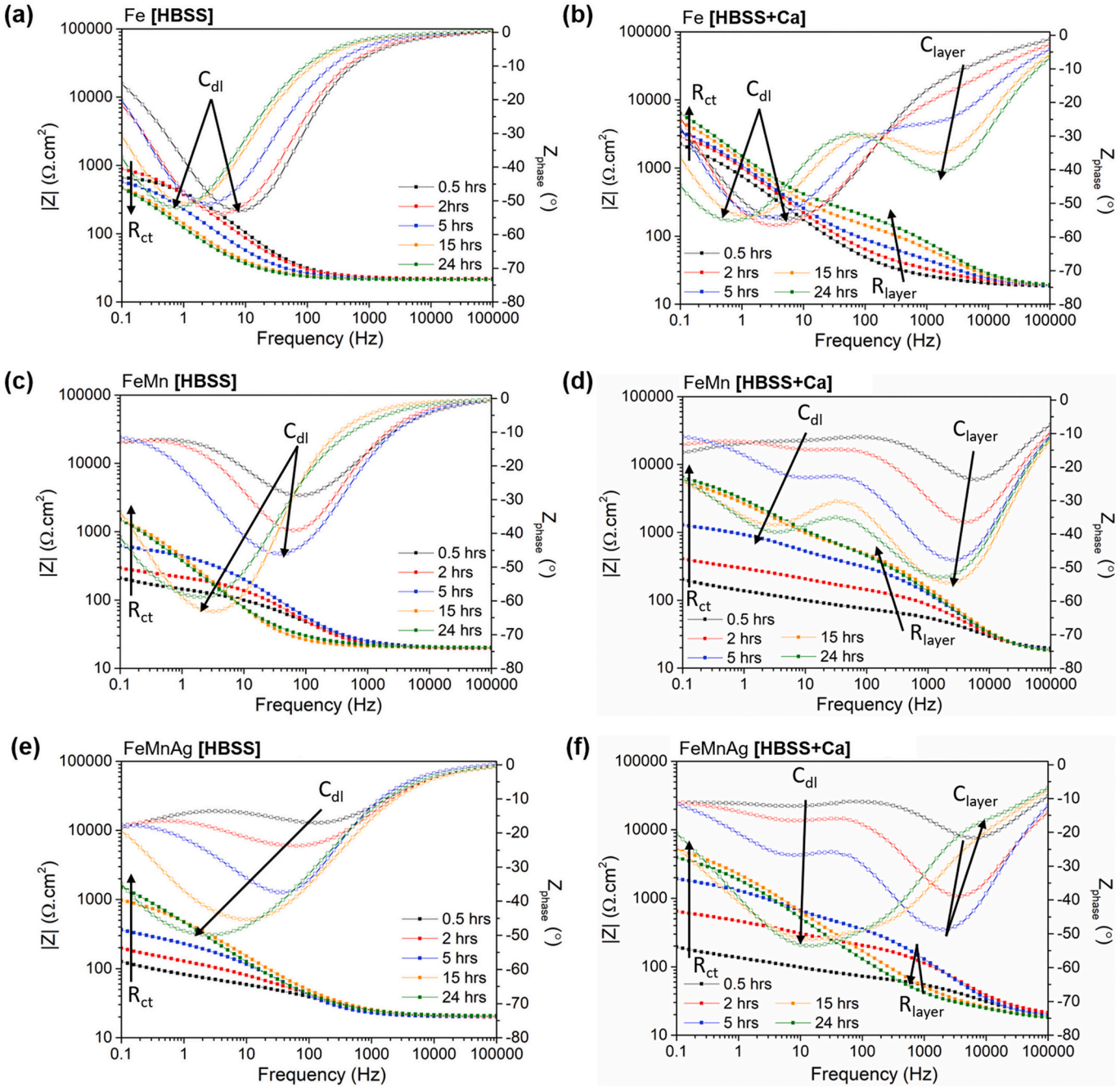

Fig. 6. EIS Bode plots for (a) Fe in HBSS (b) Fe in HBSS+Ca (c) FeMn in HBSS (d) FeMn in HBSS+Ca (e) FeMnAg in HBSS and (f) FeMnAg in HBSS+Ca. Arrows indicate features on Bode plot corresponding to equivalent circuit elements in Fig. 7b.

very small cracks, particularly next to pores (clearly seen next to the red arrow on FeMnAg in Fig. 11a and in various regions in Fig. 12), could also support this observation. The lack of phosphorus detected in such spots eliminates the possibility of this layer being Fe- or Mn-phosphate.

3.5. Local environment measurement

The local pH and dissolved oxygen (DO) evolution at the midpoint on the coupons, is shown in Fig. 13 for the first 15 min after immersion in HBSS and HBSS+Ca. Full maps measuring local environment conditions over the next 24 h are presented in Part II of this work [43]. One must keep in mind that the pH microelectrode and the oxygen micro-optode were 50 μm apart in horizontal planes and therefore the measurements recorded by the two at a given time, could be related to two slightly offset local environments. For Fe in HBSS, the pH and DO levels stabilise gradually with DO slowly being consumed and stabilising at 3.51 mg/L while pH stabilises at 7.44. On the other hand, in the case of FeMn and FeMnAg, the pH drastically increases upon immersion to around 9 and 10.5, respectively. Within 7–9 min, the pH values over both alloys decrease and stabilise at 7.38 and 7.22. The period at which the pH level recorded was high over both alloys, clearly correspond to periods of higher DO consumption. In the case of FeMn, the DO level eventually stabilised at 3.71 mg/L, while for FeMnAg, a steep decrease in DO levels led to a stabilised value of 0.53 mg/L, indicating fast oxygen reduction reaction.

When immersed in HBSS+Ca, the pH levels stabilised at 7.09, 7.28 and 7.44 for Fe, FeMn and FeMnAg respectively. Measurement of DO, reflected a totally different behaviour of the alloys in the modified

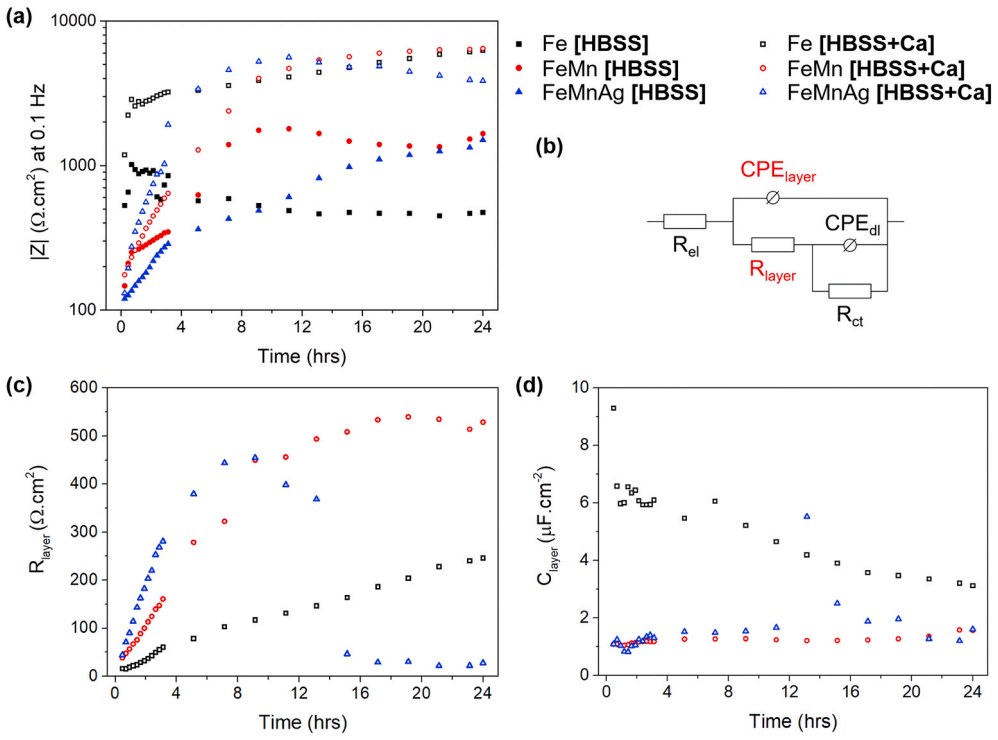

Fig. 7. (a) Development of the impedance of Fe-based alloys at 0.1 Hz in HBSS and HBSS+Ca (b) equivalent circuit used to fit spectra of metals tested in HBSS+Ca, (c) results for R_{layer} and (d) C_{layer} evolution with time based on fitting of spectra for tests conducted in HBSS+Ca.

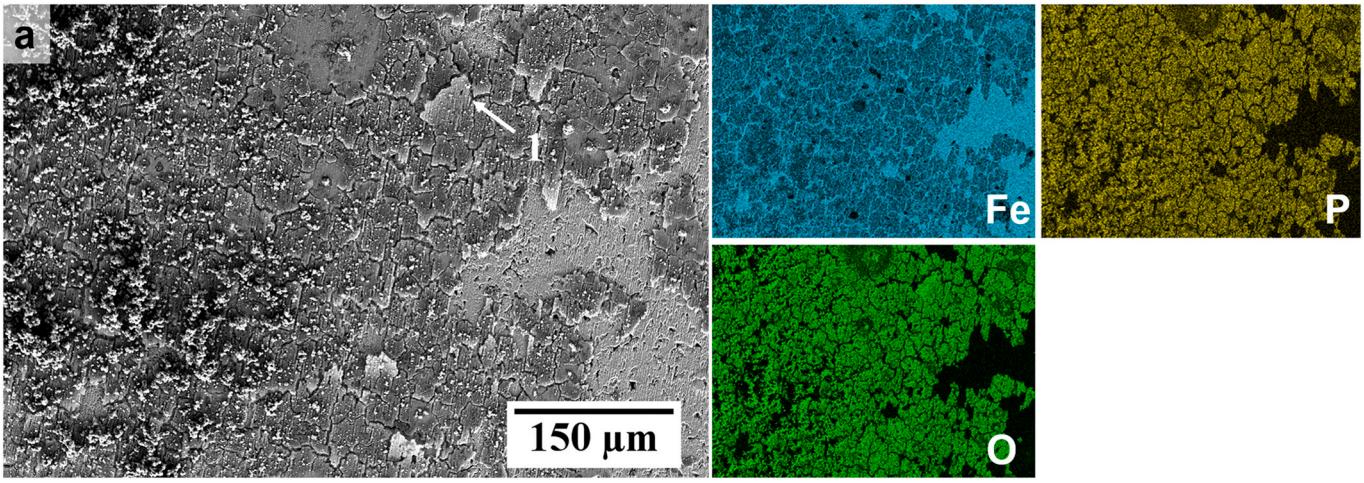

Fig. 8. SEM-EDS surface morphology of Fe immersed in HBSS for 24 h and corresponding Fe, P and O distribution maps as shown by EDS.

electrolyte. The highest recorded DO level was that for FeMnAg, at 5.00 mg/L after a steep increase over the 15-min period. For the FeMn alloy the DO level stabilised at 4.57 mg/L but briefly exhibited higher consumption upon immersion that corresponded to a slightly increased pH level. The measurements taken over the Fe coupon indicated that there was an initial period with a rather low pH (approx. 6.7) while higher consumption of DO was recoded. The DO eventually settled at 2.84 mg/L.

4. Discussion

Results from the EIS testing, clearly illustrate the impact of the testing electrolyte composition on the formation of a partially protective layer of corrosion products on the specimen surface, as evidenced by the additional time constant present at higher frequencies in Fig. 6. On the other hand, the metal composition had a direct impact on the progression of this corrosion product formation through changes in the local environment as a result of varying degradation behaviours.

In general, PDP tests indicate that FeMn and FeMnAg both corrode faster than Fe in both HBSS and HBSS+Ca. FeMnAg clearly exhibited the fastest corrosion rate in HBSS+Ca, while FeMn had higher corrosion current densities in HBSS. In general, measured i_{corr} values were higher in Ca^{2+}-free electrolyte indicating a potential presence of an active protective compound or mechanism when testing in this electrolyte. Considering the rather large scatter in measured current densities for FeMn and FeMnAg, it is likely that accelerated corrosion in the case of FeMn depends on slight compositional inhomogeneities in the austenitic phase, and/or the quantity and distribution of MnO inclusions on the tested surface [8,38,53], both of which may create localised micro-galvanic cells of varying strength. The role of MnO inclusions on the corrosion behaviour has not yet been studied despite the occurrence

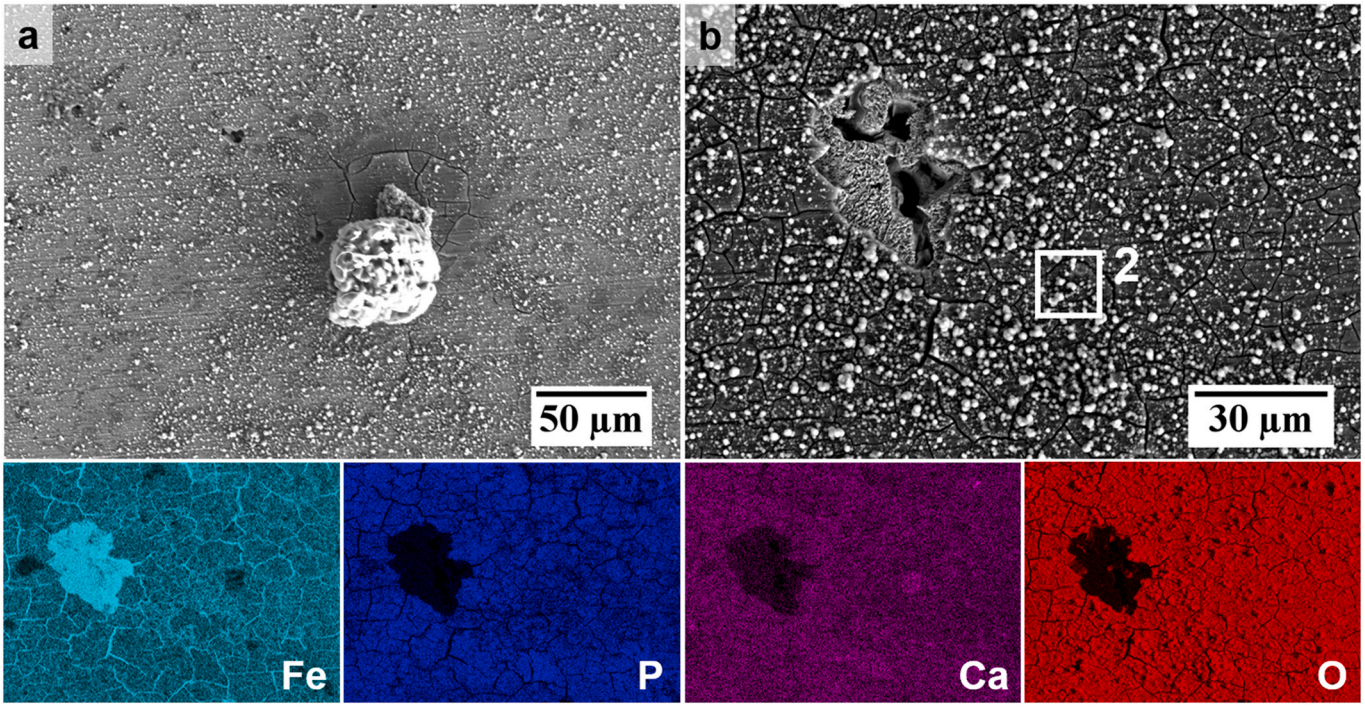

Fig. 9. (a–b) SEM-EDS surface morphology of Fe immersed in HBSS+Ca for 24 h and EDS distribution maps of Fe, P, Ca and O corresponding to the region shown in (b).

Table 2
EDS results for spot and area analysis on corrosion products in at.%.

Pt.	O	Fe	Mn	P	Ca	Na	Cl	Mg	Si	Al	Ag	N	K
1	62.40	25.20	–	08.05	–	03.56	–	00.21	00.32	00.26	–	–	–
2	58.33	25.74	–	07.63	02.03	04.35	01.32	00.36	00.24	–	–	–	–
3	23.54	46.00	25.74	01.85	–	02.87	–	–	–	–	–	–	–
4	30.20	33.04	18.81	17.24	–	00.71	–	–	–	–	–	–	–
5	46.12	21.72	18.54	09.17	01.54	02.31	–	–	–	–	–	–	00.60
6	61.04	01.16	01.48	12.58	17.15	03.02	01.71	01.86	–	–	–	–	–
7	59.08	05.93	03.06	12.62	16.30	00.32	–	02.69	–	–	–	–	–
8	08.28	58.12	31.11	00.88	01.03	00.20	–	00.38	–	–	–	–	–
9	66.18	03.98	18.40	09.33	00.46	01.19	00.46	–	–	–	–	–	–
10	69.73	12.42	09.26	05.86	–	01.93	00.13	–	–	–	00.67	–	–
11	68.89	00.53	00.62	10.96	16.12	00.34	–	02.49	00.05	–	–	–	–
12	52.28	16.94	09.26	08.69	09.76	00.13	–	02.76	00.18	–	–	–	–
γ-FeMn region before test	02.84	57.02	27.86	–	–	–	–	–	00.44	–	–	11.84	–

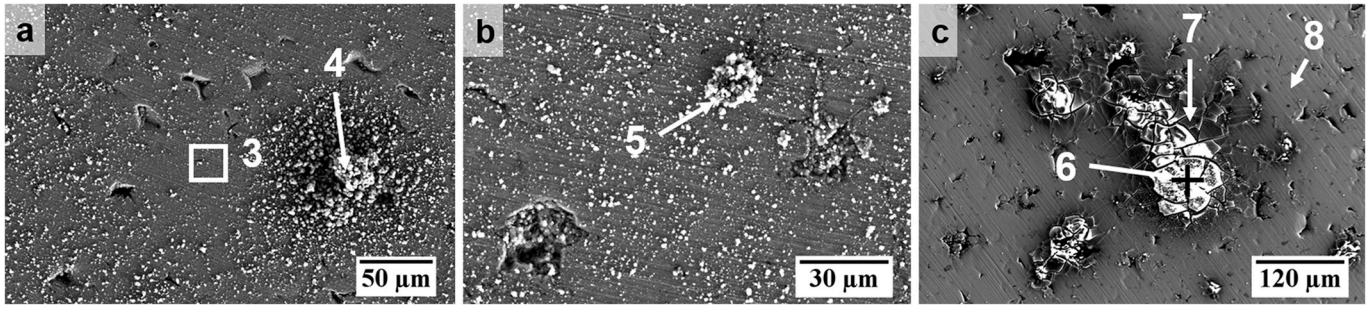

Fig. 10. SEM surface morphology of FeMn immersed in HBSS (a–b) and HBSS+Ca (c) with points for EDS analysis.

of the oxide in most powder-processed FeMn microstructures, however Hermawan et al. [7] have mentioned its potential to accelerate corrosion as a cathode in an FeMn matrix. While the austenite Fe:Mn ratio and fluctuations in the test surface area could be quantified or estimated (Fig. 2), the variation in quantity of MnO inclusions in any given area cannot be similarly quantified. This could therefore be a major contributor to the scatter in measured currents for FeMn and FeMnAg alloys. Like FeMn, the FeMnAg alloy also has similar compositional and percentage pore variations, and the MnO phase is similarly present within the microstructure, however the presence of the Ag is likely to be

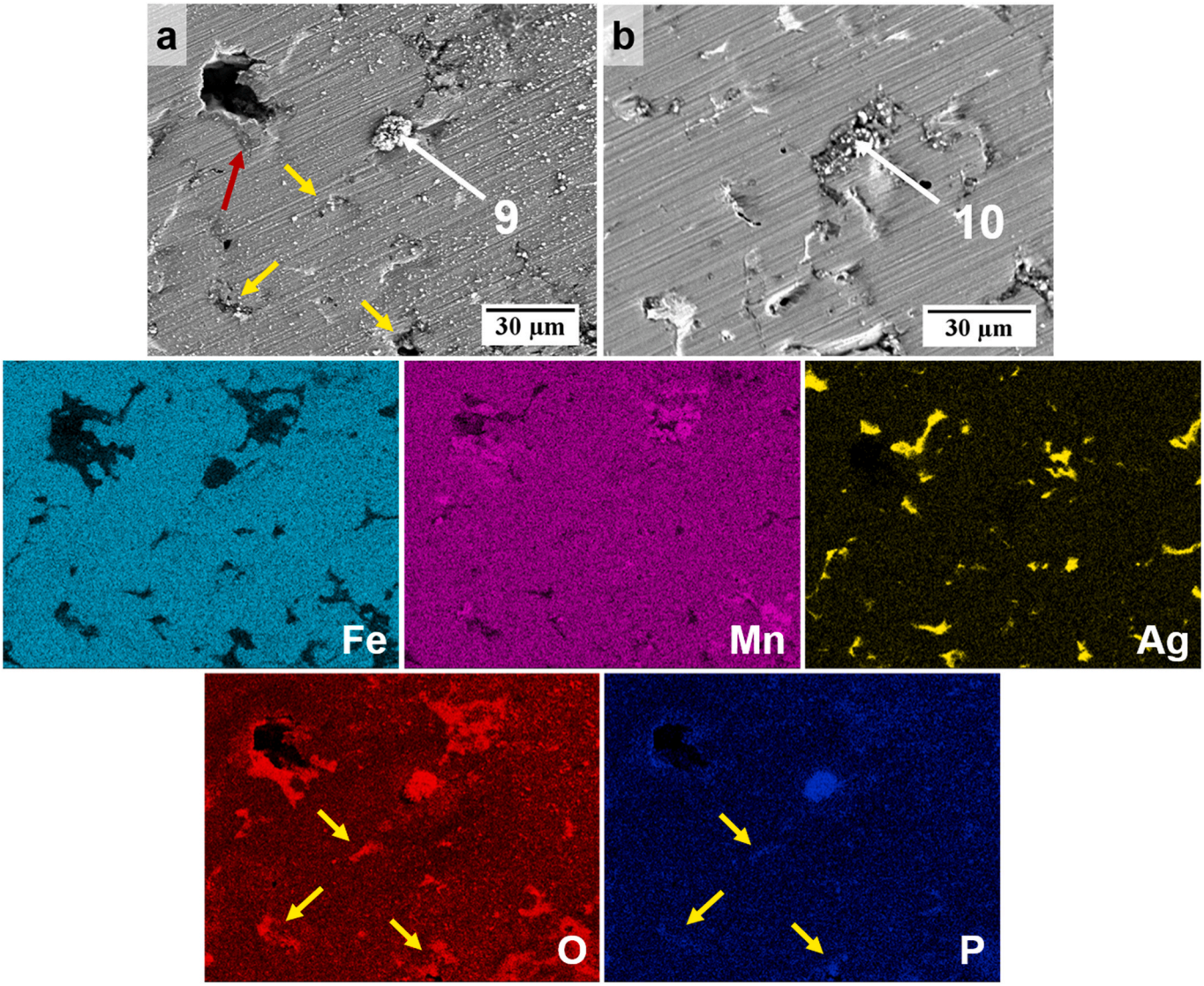

Fig. 11. (a–b) SEM-EDS surface morphology of FeMnAg immersed in HBSS for 24 h. EDS maps correspond to distribution maps of Fe, Mn, Ag, O and P in the region shown in (a). The red arrow points towards cracks indicating presence of a thin layer of corrosion product. Yellow arrows show evidence of phosphate compounds in selected pores.

more effective in corrosion acceleration as shown when testing in HBSS+Ca. In this case the Ag phase also acted as a cathode while the FeMn matrix served as the anode, as likewise observed in other Ag-containing Fe alloys [25,40,54,55]. On the other hand, when testing in HBSS, it is possible that considerable ferrous (Fe^{2+}) and ferric (Fe^{3+}) compounds formed on the surface of FeMnAg after 1 h, as indicated in optical images presented in Part II of this work [43], and limited the measured corrosion current.

Alternative means of corrosion rate approximation, particularly weight-loss measurements, were considered to provide an indication of corrosion performance at freely corroding conditions. However, considering the material characterisation presented in Fig. 3, the amount of MnO inclusions visible at the polished surface and within unspecified pore areas, was expected to present difficulties in finding an etchant solution that preferentially removes corrosion products without altering any constituent of the underlying material. In particular, several cleaning solutions suggested in the ASTM G1 standard [56] for cleaning of corrosion-tested iron and steel, including the addition of 3.5 g/L hexamethylenetetramine to a 6 M HCl solution as well as different concentrations of zinc chips in diluted NaOH, were not effective in providing a consistent performance when testing blank i.e. untested, FeMn coupons. Preferential attack of either oxide inclusions, or the FeMn phase was observed. For a testing period of 24 h, as was the interest in the context of this study, the error from substrate attack would have led to considerable uncertainty on the corrosion results presented.

4.1. *Corrosion behaviour of Fe and Fe-alloys in Ca^{2+}-free HBSS*

The addition of Mn to Fe clearly led to significantly different starting behaviour when testing in HBSS compared to pure Fe (Fig. 13). The initial local changes in pH and DO observed at the surface of Fe seem to indicate that there was no accelerated corrosion operating as both DO and pH levels stabilised gradually towards the bulk conditions over the first 15 min. On the other hand, the significant spike in pH for Mn-containing alloys may suggest an initially strong cathodic reaction of oxygen reduction (reaction **2**), supported by the corresponding DO consumption before both values also stabilise rather rapidly to bulk conditions. The addition of Ag to the alloy clearly triggered an accelerated micro-galvanic corrosion as DO levels dropped drastically to 0.53 mg/L after just 700 s, indicating a rapidly progressing corrosion process, oxygen-diffusion limited, as further confirmed in Part II of this work [43]. The behaviour of the alloys in HBSS suggests that no significant

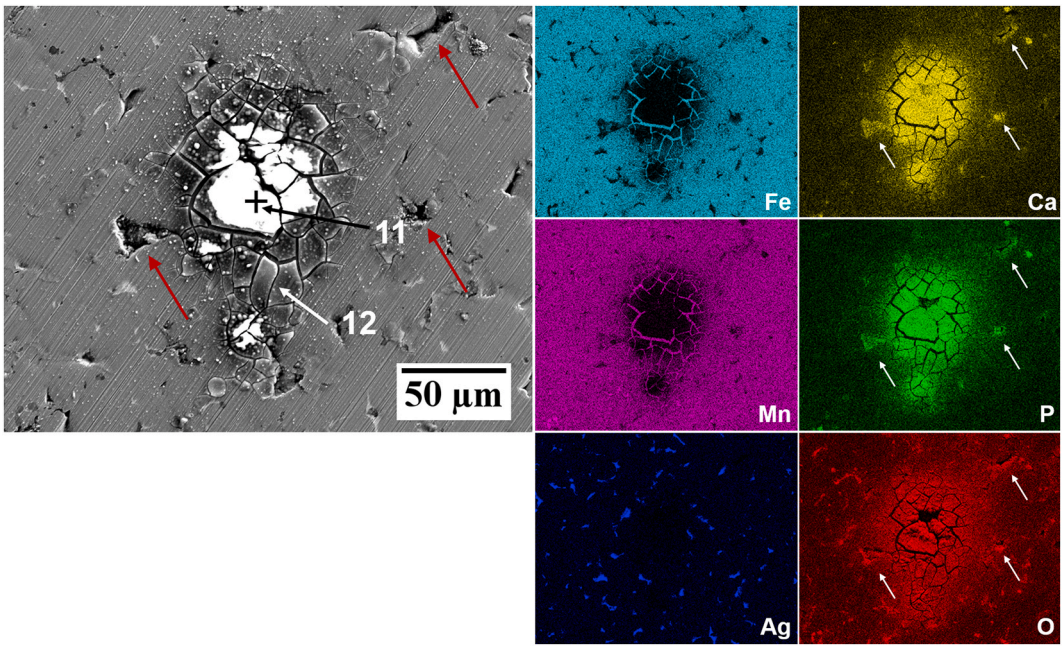

Fig. 12. SEM-EDS surface morphology of FeMnAg immersed in HBSS+Ca for 24 h. EDS maps correspond to the Fe, Mn, Ag, Ca, P and O distribution maps for the region shown in the micrograph. Unlabelled arrows provide reference points for selected pore locations.

barrier to corrosion was present in the form of corrosion products or protective precipitates on the surface of the alloys in the initial moments following immersion. This is further supported by the absence of the time constant at high frequencies in the initial and consequent EIS scans.

Hydra-Medusa software [57], was used to indicate how precipitate formation may change with different electrolyte constituents by using the Hydra thermodynamic stability constant database to plot equilibrium diagrams of specific ion concentrations against pH. The concentration of Fe^{2+} and Mn^{2+} present was set at 1.00 mM and 0.35 mM respectively in the chemical simulations based on the compositional ratio in the alloys. Oxidation rate of Fe^{2+} to Fe^{3+} increases at higher pH and sufficient oxygen concentration, thus, an additional equilibrium system containing 1.00 mM of Fe^{3+} was also calculated. These may appear to be relatively high concentrations when compared to figures reported in literature for ion concentrations measured in electrolyte post-immersion testing [37,58–61]. However, one must consider that these values correspond to bulk concentrations. The concentration of ions originating from local degradation reactions and being used in the precipitation of products, are significantly larger. In fact, the products observed were detected by multiple authors testing in similar electrolyte formulations after several days of immersion and significant corrosion product formation [26,34,38]. Nonetheless, the MEDUSA simulations presented in Fig. 14, may be used as guidelines if interpreted with these limitations in mind and supported by other results. The electrolyte formulations used for the simulations, are given in Table 3.

Based on the Medusa diagrams, the precipitate products on Fe alloys in HBSS could be $Fe_3(PO_4)_2{\cdot}8H_2O$, $MnHPO_4$, $FeCO_3$ and $Fe(OH)_{2.7}Cl_{0.3}$ (Fig. 14a–b), although higher localised concentrations of Mn^{2+} could also support the formation of $MnCO_3$ based on supporting Medusa diagrams. EDS mapping of the corrosion products on Fe (Fig. 8), indicate that the 'flaky' layer is likely to be a similar Fe-phosphate product corresponding to the result in Fig. 14a. Mouzou et al. [34] reported the presence of $MnCO_3$ on Fe–20Mn–1C alloys tested in HBSS with and without Ca^{2+}. With the increase of CO_3^{2-} concentration in the bulk electrolytes, the increment of $MnCO_3$ was found to significantly decrease the corrosion rate. However, in our work, $MnCO_3$ was most likely absent based on EDS results in Fig. 10a–b and Fig. 11, and the precipitation of Mn-phosphates seems to be dominant. Incidentally, the increase of Mn^{2+} concentration in the electrolyte decreases the precipitation of the Fe-phosphates based on supporting Medusa diagrams, indicating a higher tendency for Mn-phosphates to precipitate over Fe-phosphates. This explains why the 'flaky' product observed on Fe alloys was not evident on FeMn and FeMnAg.

The monitoring of the low frequency impedance magnitude, as illustrated in Fig. 7a, provides information on changing conditions at the metal-electrolyte interface as a result of progressing corrosion. The starting impedance is considerably higher for Fe compared to the FeMn alloys. This corroborates the results in literature [21,23,25,26,40] and is related to better protective properties of the native oxide film. An increase in the impedance of FeMn and FeMnAg could be related to the formation of oxides/hydroxides from interactions between Fe^{2+}/Fe^{3+} ions with generated OH^-. Similar EIS results were obtained in a study on the corrosion of low carbon steel in 3% NaCl wherein the formation of oxide/hydroxide layers also led to a single time-constant diffusion-controlled system [62]. Higher concentrations of oxygen on the seemingly bare-metal surface and the small cracks near pores (Fig. 10a), confirm the presence of a thin layer of additional corrosion product adjacent to the surface.

4.2. Corrosion behaviour of Fe and Fe-alloys in Ca^{2+}-containing HBSS

The Medusa diagrams reflecting potential products in HBSS+Ca (Fig. 14c–d) indicate that apart from the possible precipitates mentioned previously, $Ca_{10}(PO_4)_6(OH)_2$, $CaCO_3$ and $CaSO_4$ are other potential precipitates. In fact, when analysing the results for initial local measurements presented in Fig. 13 for tests conducted in HBSS+Ca, the pH changes are generally opposite those for tests carried out in HBSS. Whereas precipitation of Fe- and Mn-phosphates requires only the metal cations and PO_4^{3-} in solution (reaction **5**), the precipitation of $Ca_{10}(PO_4)_6(OH)_2$ in HBSS+Ca requires OH^- ions (reaction **6**) generated in the oxygen reduction reaction (reaction **2**) [63].

$$3Fe^{2+} + 2PO_4^{3-} + 8H_2O \rightarrow Fe_3(PO_4)_2.8H_2O \quad (5)$$

$$6PO_4^{3-} + 10Ca^{2+} + 2OH^- \rightarrow Ca_{10}(PO_4)_6(OH)_2 \quad (6)$$

The local pH and DO response for FeMnAg in particular, seems to indicate an initial high consumption of DO, as expected from the micro-galvanic reaction described previously. This also resulted in rather

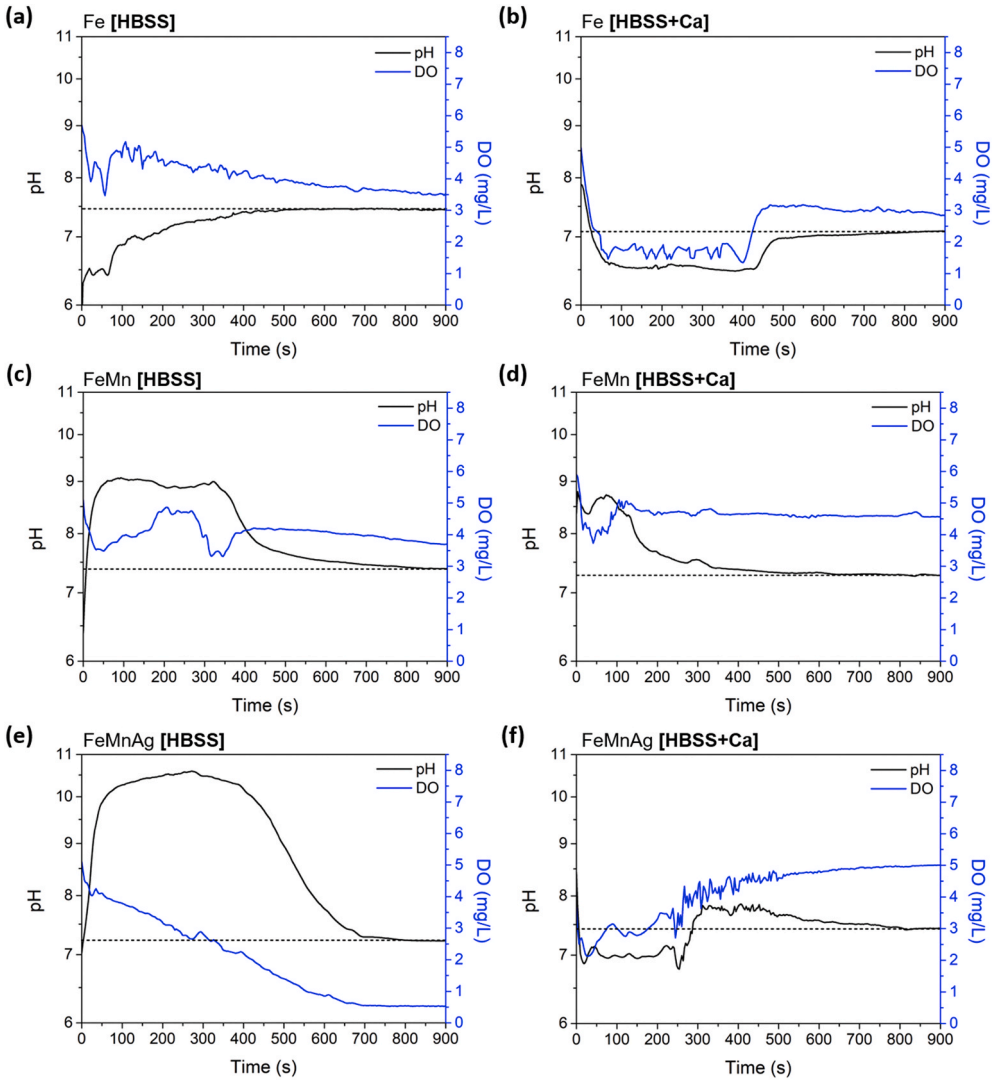

Fig. 13. Monitoring of local pH and DO levels in the first 15 min upon immersion of (a) Fe in HBSS (b) Fe in HBSS+Ca (c) FeMn in HBSS (d) FeMn in HBSS+Ca (e) FeMnAg in HBSS and (f) FeMnAg in HBSS+Ca. The dashed line indicates the value at which the pH settles in each test.

neutral pH levels, due to the immediate use of the generated OH^- for precipitate formation. The formed layer could then have reduced the oxygen reduction rate at that point, accounting for the recorded DO of 5.00 mg/L and stabilised pH level (Fig. 13f) [64]. In the case of FeMn, the slight increase in DO consumption corresponding to an increase in pH in the initial minutes also indicates an initial cathodic reaction that is sustained for a shorter period of time than in HBSS. The pH level then stabilises as the Ca/P products precipitate. In contrast, the measurements taken at the Fe surface seem to point towards a rather prolonged cathodic reaction compared to the FeMn-alloys. This is further supported by the fact that based on PDP results, where Fe exhibits a slower corrosion rate, and therefore could sustain a more gradual cathodic reaction and simultaneous precipitation of Ca/P products. In general, the fast accumulation of Ca/P-rich products could also be reflected in the immediate phase shift evident for all alloys to different degrees within the first 30 min in Fig. 6 and the increase in calculated corrosion layer resistance, R_{layer} in Fig. 7c. The decrease in capacitance values corresponding to the capacitive contribution of the corrosion product layer shown in Fig. 7d is also typical of increasing formation of corrosion products, as also observed by Schinhammer et al. [13] with Fe–21Mn-0.7C and Fe–21Mn-0.7C–1Pd samples in SBF. Although FeMnAg had the steepest initial increase in R_{layer}, and used OH^- from the oxygen reduction rate for rapid precipitation of Ca/P products, PDP results still indicate that this alloy corroded the fastest in HBSS+Ca. The complete coverage of the FeMnAg in HBSS+Ca could also be clearly seen by the stable and rather uniform measurement of DO over the sample surface in Part II of this work, while corresponding pH measurements over the 24 h period remained at neutral levels. Despite the resistance contribution from the corrosion precipitate layer, results presented in Part II of this work [43] clearly show that diffusion of DO was possible as DO levels continued decreasing over the course of 24 h. The cathodic oxygen reduction reaction was not completely suffocated, allowing for further generation of OH^- and growth of the time constant corresponding to the same precipitate layer. In the Bode plots for FeMn and FeMnAg (Fig. 6d and **f**), one could also observe the growth of the initial time constant, indicating potential formation and evolution of thin hydroxide layers at the surface as described for the materials tested in HBSS (Fig. 11).

Corrosion product analysis for the materials tested in HBSS+Ca, confirm the presence of the Ca/P-rich products over all samples. Despite the rather considerable growth of the high-frequency time constant, and evidence of more complete coverage of sample surface with bright products in the 24-h localised corrosion testing, the presence of the Ca/P products on FeMn and FeMnAg were rather localised. This could be due to the less-adherent precipitates being dislodged during the rinsing of the samples prior to SEM analysis. The evidence of phosphates in the

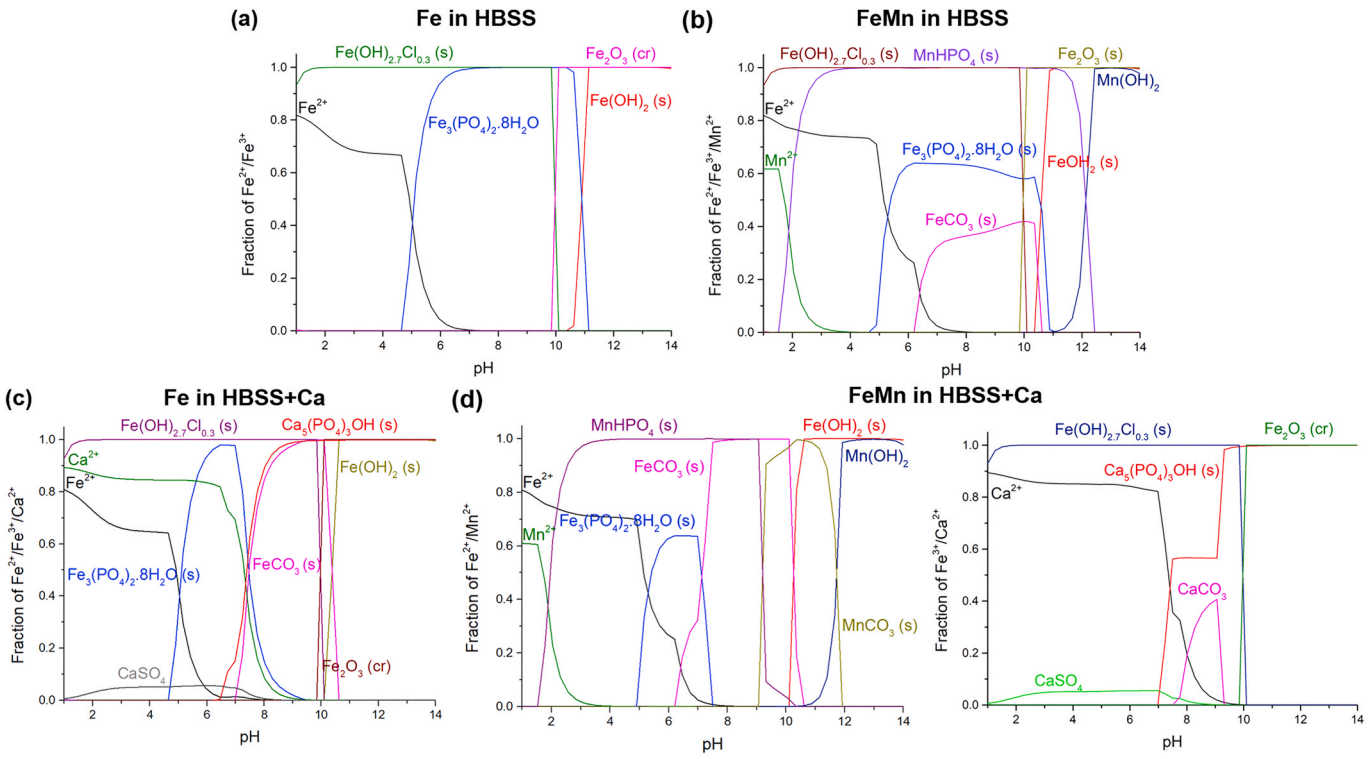

Fig. 14. Fraction of Fe^{2+}, Fe^{3+}, Mn^{2+} and Ca^{2+} with other species present in the electrolyte based on the constituents of (a–b) HBSS and (c–d) HBSS+Ca. The simulations were carried out by Hydra-Medusa. The complete formulations used in the simulations are given in Table 3.

Table 3
Electrolyte formulations used in MEDUSA simulations in Fig. 14.

Constituent (mM)	(a) Fe in HBSS	(b) FeMn in HBSS (b)	(c) Fe in HBSS+Ca	(d) FeMn in HBSS+Ca
Fe^{2+}	1.00	1.00	1.00	1.00
Fe^{3+}	1.00	1.00	1.00	1.00
Mn^{2+}	–	0.35	–	0.35
Ca^{2+}	–	–	1.26	1.26
Mg^{2+}	–	–	0.90	0.90
K^{+}	5.77	5.77	5.77	5.77
Na^{+}	142.77	142.77	142.77	142.77
HPO_4^{2-}	0.78	0.78	0.78	0.78
HCO^{3-}	4.17	4.17	4.17	4.17
Cl^{-}	143.26	143.26	146.77	146.77
SO_4^{2-}	–	–	0.41	0.41

pores could be a further reflection of this, as pores are generally more difficult to remove products from. The cracked product underneath the isolated Ca/P deposits could be metal hydroxide that form preferentially adjacent to oxygen-deficient areas due to slightly localised corrosion in the form of pitting, or in this case, enlargement of existent pores. Over the Fe sample, the Fe-phosphate layer was still evident apart from the Ca/P products. Similarly, the Fe-phosphate layer, while providing no solid barrier to ion transfer, still allowed for conditions favourable for localised pits to form underneath, as observed in Fig. 9.

An interesting development in the mid-range frequency impedance in the Bode plot for FeMnAg alloy, is that following the rapid initial increase in corrosion layer resistance recorded, the protective characteristic of the precipitate layer seemed to decrease with time. This was observed in the sudden decrease and increase of the R_{layer} and C_{layer} values respectively (Fig. 7c–d), after approximately 9 h of immersion. This could suggest a change in the inherent structure, loss of layer uniformity, development of a porous morphology or some other form of breach experienced by the protective layer. The consequent decrease in capacitance indicates that the layer started to gradually regain some of its integrity without attaining considerable resistance. Results from the 24-h local measurement presented in Part II [43] also show that DO consumption increased after several hours for FeMnAg. This may indicate that although the Ca^{2+} ions present in solution definitely influence the corrosion rate, more significant deceleration and blocking of electrochemically active species from the metal surface reported in previous *in vivo* studies [3,19,35,36], is more likely due to the formation of compact oxides and hydroxides that develop over longer immersion periods, especially in the case of Fe-alloys in Ca^{2+}-containing environment.

5. Conclusion

General and localised *in vitro* corrosion testing methods were utilised in order to study the effect of HBSS testing electrolyte, with and without added Ca^{2+} ions, on the corrosion of Fe, Fe35Mn and (Fe35Mn)5Ag alloys for biodegradable implant applications, over a 24-h period. The main conclusions may be summarised as follows:

1) Partial protection from corrosion in HBSS+Ca was confirmed for Fe, FeMn and FeMnAg in potentiodynamic polarisation tests in which the alloys generated lower corrosion current densities compared to that in Ca^{2+}-free HBSS.
2) FeMnAg exhibited the highest corrosion current density compared to pure Fe and FeMn in Ca^{2+}-containing HBSS, despite having the steepest increase in resistance associated with the Ca/P layer, indicating the positive effect of a noble-phase addition on accelerating corrosion in the more representative electrolyte for orthopaedic implantation sites.
3) The presence of Ca^{2+} in HBSS resulted in the formation of a partially protective Ca/P-rich precipitate which was visually observed on the sample surface but also clearly evident as an additional time constant at around 1500 Hz in EIS Bode plots, even after the initial 30 min. The growth of the Ca/P-rich layer was not consistent over the initial 24-h period on the FeMnAg sample in HBSS+Ca, as a decrease in the layer resistance was affected after approximately 9 h.

4) Precipitation of Mn-phosphates was more dominant in corroding FeMn and FeMnAg as the prominent Fe-phosphate layer present on corroding Fe samples was absent on both FeMn and FeMnAg, in both electrolytes. Both Fe- and Mn-phosphates did not offer significant protection compared to Ca-phosphates.
5) Local pH and DO measurements in the first 15 min following immersion, indicated a strong cathodic oxygen reduction reaction on FeMnAg in HBSS, making progressing corrosion oxygen diffusion limited. Contrarily, measurements on FeMn and FeMnAg in HBSS+Ca indicated a slower cathodic reaction due to the protective effect of forming precipitates.

This study has highlighted the contrasting behaviour of Fe-based materials of interest in the biodegradable metals field, when tested in two common electrolytes, indicating the importance of conducting tests in representative testing solutions.

CRediT authorship contribution statement

Christabelle Tonna: Data curation, Visualization, Formal analysis, Investigation, Writing – original draft, Writing – review & editing. **Cheng Wang:** Data curation, Formal analysis, Investigation, Writing – original draft, Writing – review & editing. **Di Mei:** Investigation, Writing – review & editing. **Sviatlana V. Lamaka:** Conceptualization, Supervision, Writing – review & editing. **Mikhail L. Zheludkevich:** Conceptualization, Supervision, Writing – review & editing. **Joseph Buhagiar:** Conceptualization, Supervision, Writing – review & editing.

Declaration of competing interest

The authors declare that they have no competing interests.

Acknowledgements

Christabelle Tonna and Joseph Buhagiar would like to thank the Malta Council for Science and Technology, for funding Project BioSA (R&I-2017-037-T) through the FUSION: R&I Technology Development Programme. Cheng Wang thanks the China Scholarship Council for the award of fellowship and funding (No. 201806310128).

Appendix A. Supplementary data

Supplementary data to this article can be found online at https://doi.org/10.1016/j.bioactmat.2021.05.048.

References

[1] E. Cerrato, U. Barbero, J.A.G. Romero, GiorgioQuadri, H. Mejia-Renteria, F. Tomassini, et al., Magmaris™ resorbable magnesium scaffold: state-of-art review, Future Cardiol. 15 (2019) 267–279, https://doi.org/10.2217/fca-2018-0081.
[2] K. Kumar, R.S. Gill, U. Batra, Challenges and opportunities for biodegradable magnesium alloy implants, Mater. Technol. 33 (2018) 153–172, https://doi.org/10.1080/10667857.2017.1377973.
[3] M. Peuster, P. Wohlsein, M. Brügmann, M. Ehlerding, K. Seidler, C. Fink, et al., A novel approach to temporary stenting: degradable cardiovascular stents produced from corrodible metal—results 6–18 months after implantation into New Zealand white rabbits, Heart 86 (2001) 563–569, https://doi.org/10.1136/heart.86.5.563.
[4] G. Katarivas Levy, J. Goldman, E. Aghion, The prospects of zinc as a structural material for biodegradable implants—a review paper, Metals 7 (2017) 402.
[5] J. He, F.-L. He, D.-W. Li, Y.-L. Liu, Y.-Y. Liu, Y.-J. Ye, et al., Advances in Fe-based biodegradable metallic materials, RSC Adv. 6 (2016), https://doi.org/10.1039/C6RA20594A.
[6] H. Hermawan, D. Dubé, D. Mantovani, Development of degradable Fe-35Mn alloy for biomedical application, Adv. Mater. Res. 15–17 (2006) 107–112. https://doi.org/10.4028/www.scientific.net/AMR.15-17.107.
[7] H. Hermawan, H. Alamdari, D. Mantovani, D. Dubé, Iron–manganese: new class of metallic degradable biomaterials prepared by powder metallurgy, Powder Metall. 51 (2008) 38–45, https://doi.org/10.1179/174329008X284868.
[8] H. Hermawan, D. Dube, D. Mantovani, Degradable metallic biomaterials: design and development of Fe-Mn alloys for stents, J. Biomed. Mater. Res. A. 93 (2010) 1–11, https://doi.org/10.1002/jbm.a.32224.
[9] H. Hermawan, D. Mantovani, Process of prototyping coronary stents from biodegradable Fe-Mn alloys, Acta Biomater. 9 (2013) 8585–8592, https://doi.org/10.1016/j.actbio.2013.04.027.
[10] H. Hermawan, A. Purnama, D. Dube, J. Couet, D. Mantovani, Fe–Mn alloys for metallic biodegradable stents: degradation and cell viability studies, Acta Biomater. 6 (2010) 1852–1860, https://doi.org/10.1016/j.actbio.2009.11.025.
[11] M. Schinhammer, A.C. Hanzi, J.F. Loffler, P.J. Uggowitzer, Design strategy for biodegradable Fe-based alloys for medical applications, Acta Biomater. 6 (2010) 1705–1713, https://doi.org/10.1016/j.actbio.2009.07.039.
[12] M. Schinhammer, I. Gerber, A.C. Hanzi, P.J. Uggowitzer, On the cytocompatibility of biodegradable Fe-based alloys, Mater. Sci. Eng. C 33 (2013) 782–789, https://doi.org/10.1016/j.msec.2012.11.002.
[13] M. Schinhammer, P. Steiger, F. Moszner, J.F. Loffler, P.J. Uggowitzer, Degradation performance of biodegradable Fe-Mn-C(-Pd) alloys, Mater. Sci. Eng. C 33 (2013) 1882–1893, https://doi.org/10.1016/j.msec.2012.10.013.
[14] J. Čapek, S. Msallamová, E. Jablonská, J. Lipov, D. Vojtěch, A novel high-strength and highly corrosive biodegradable Fe-Pd alloy: structural, mechanical and in vitro corrosion and cytotoxicity study, Mater. Sci. Eng. C 79 (2017) 550–562, https://doi.org/10.1016/j.msec.2017.05.100.
[15] M. Moravej, A. Purnama, M. Fiset, J. Couet, D. Mantovani, Electroformed pure iron as a new biomaterial for degradable stents: in vitro degradation and preliminary cell viability studies, Acta Biomater. 6 (2010) 1843–1851, https://doi.org/10.1016/j.actbio.2010.01.008.
[16] A. Orinak, R. Oriňáková, Z. Orsagova Kralova, A. Morovska Turonova, M. Kupková, M. Hrubovčáková, et al., Sintered metallic foams for biodegradable bone replacement materials, J. Porous Mater. (2014) 21, https://doi.org/10.1007/s10934-013-9757-4.
[17] E. Zhang, H. Chen, F. Shen, Biocorrosion properties and blood and cell compatibility of pure iron as a biodegradable biomaterial, J. Mater. Sci. Mater. Med. 21 (2010) 2151–2163, https://doi.org/10.1007/s10856-010-4070-0.
[18] S. Zhu, N. Huang, L. Xu, Y. Zhang, H. Liu, H. Sun, et al., Biocompatibility of pure iron: in vitro assessment of degradation kinetics and cytotoxicity on endothelial cells, Mater. Sci. Eng. C 29 (2009) 1589–1592, https://doi.org/10.1016/j.msec.2008.12.019.
[19] A. Drynda, T. Hassel, F.W. Bach, M. Peuster, In vitro and in vivo corrosion properties of new iron-manganese alloys designed for cardiovascular applications, J. Biomed. Mater. Res. B Appl. Biomater. 103 (2015) 649–660, https://doi.org/10.1002/jbm.b.33234.
[20] B. Liu, Y.F. Zheng, Effects of alloying elements (Mn, Co, Al, W, Sn, B, C and S) on biodegradability and in vitro biocompatibility of pure iron, Acta Biomater. 7 (2011) 1407–1420, https://doi.org/10.1016/j.actbio.2010.11.001.
[21] M.S. Dargusch, A. Dehghan-Manshadi, M. Shahbazi, J. Venezuela, X. Tran, J. Song, et al., Exploring the role of manganese on the microstructure, mechanical properties, biodegradability, and biocompatibility of porous iron-based scaffolds, ACS Biomater. Sci. Eng. 5 (2019) 1686–1702, https://doi.org/10.1021/acsbiomaterials.8b01497.
[22] M. Dehestani, K. Trumble, H. Wang, H. Wang, L.A. Stanciu, Effects of microstructure and heat treatment on mechanical properties and corrosion behavior of powder metallurgy derived Fe–30Mn alloy, Mater. Sci. Eng. A 703 (2017) 214–226, https://doi.org/10.1016/j.msea.2017.07.054.
[23] C. Shuai, W. Yang, Y. Yang, H. Pan, C. He, F. Qi, et al., Selective laser melted Fe-Mn bone scaffold: microstructure, corrosion behavior and cell response, Mater. Res. Express 7 (2020), 015404, https://doi.org/10.1088/2053-1591/ab62f5.
[24] M. Kupkova, M. Hrubovcakova, M. Kupka, R. Orinakova, A. Morovska Turonova, Sintering behaviour, graded microstructure and corrosion performance of sintered Fe-Mn biomaterials, Int. J. Electrochem. Sci. 10 (2015) 9256–9268.
[25] P. Sotoudeh Bagha, M. Khakbiz, S. Sheibani, H. Hermawan, Design and characterization of nano and bimodal structured biodegradable Fe-Mn-Ag alloy with accelerated corrosion rate, J. Alloys Compd. 767 (2018) 955–965, https://doi.org/10.1016/j.jallcom.2018.07.206.
[26] S. Loffredo, C. Paternoster, N. Giguère, M. Vedani, D. Mantovani, Effect of silver on corrosion behavior of plastically deformed twinning-induced plasticity steel for biodegradable stents, JOM (2020), https://doi.org/10.1007/s11837-020-04111-w.
[27] Q. Zhang, P. Cao, Degradable porous Fe-35wt.%Mn produced via powder sintering from NH4HCO3 porogen, Mater. Chem. Phys. 163 (2015) 394–401.
[28] D. Carluccio, C. Xu, J. Venezuela, Y. Cao, D. Kent, M. Bermingham, et al., Additively manufactured iron-manganese for biodegradable porous load-bearing bone scaffold applications, Acta Biomater. 103 (2020) 346–360, https://doi.org/10.1016/j.actbio.2019.12.018.
[29] M. Heiden, E. Walker, E. Nauman, L. Stanciu, Evolution of novel bioresorbable iron-manganese implant surfaces and their degradation behaviors in vitro, J. Biomed. Mater. Res. A. 103 (2015) 185–193, https://doi.org/10.1002/jbm.a.35155.
[30] N.B. Sing, A. Mostavan, E. Hamzah, D. Mantovani, H. Hermawan, Degradation behavior of biodegradable Fe35Mn alloy stents, J. Biomed. Mater. Res. B Appl. Biomater. 103 (2015) 572–577, https://doi.org/10.1002/jbm.b.33242.
[31] B. Liu, Y.F. Zheng, L. Ruan, In vitro investigation of Fe30Mn6Si shape memory alloy as potential biodegradable metallic material, Mater. Lett. 65 (2011) 540–543, https://doi.org/10.1016/j.matlet.2010.10.068.
[32] M. Caligari Conti, D. Aquilina, C. Paternoster, D. Vella, E. Sinagra, D. Mantovani, et al., Influence of cold rolling on in vitro cytotoxicity and electrochemical behaviour of an Fe-Mn-C biodegradable alloy in physiological solutions, Heliyon 4 (2018), e00926, https://doi.org/10.1016/j.heliyon.2018.e00926.

[33] D. Mei, C. Wang, S.V. Lamaka, M.L. Zheludkevich, Clarifying the influence of albumin on the initial stages of magnesium corrosion in Hank's balanced salt solution, J. Magnes. Alloy (2020), https://doi.org/10.1016/j.jma.2020.07.002.
[34] E. Mouzou, C. Paternoster, R. Tolouei, A. Purnama, P. Chevallier, D. Dube, et al., In vitro degradation behavior of Fe-20 Mn-1.2C alloy in three different pseudo-physiological solutions, Mater. Sci. Eng. C 61 (2016) 564–573, https://doi.org/10.1016/j.msec.2015.12.092.
[35] T. Kraus, F. Moszner, S. Fischerauer, M. Fiedler, E. Martinelli, J. Eichler, et al., Biodegradable Fe-based alloys for use in osteosynthesis: outcome of an in vivo study after 52 weeks, Acta Biomater. 10 (2014) 3346–3353, https://doi.org/10.1016/j.actbio.2014.04.007.
[36] M. Traverson, M. Heiden, L.A. Stanciu, E.A. Nauman, Y. Jones-Hall, G.J. Breur, In vivo evaluation of biodegradability and biocompatibility of Fe30Mn alloy, Vet. Comp. Orthop. Traumatol. 31 (2018) 10–16, https://doi.org/10.3415/vcot-17-06-0080.
[37] J. Čapek, K. Stehlíková, A. Michalcová, Š. Msallamová, D. Vojtěch, Microstructure, mechanical and corrosion properties of biodegradable powder metallurgical Fe-2 wt% X (X = Pd, Ag and C) alloys, Mater. Chem. Phys. 181 (2016) 501–511, https://doi.org/10.1016/j.matchemphys.2016.06.087.
[38] A. Gebert, F. Kochta, A. Voß, S. Oswald, M. Fernandez-Barcia, U. Kühn, et al., Corrosion studies on Fe-30Mn-1C alloy in chloride-containing solutions with view to biomedical application, Mater. Corros. 69 (2018) 167–177, https://doi.org/10.1002/maco.201709476.
[39] D. Mei, S.V. Lamaka, X. Lu, M.L. Zheludkevich, Selecting medium for corrosion testing of bioabsorbable magnesium and other metals – a critical review, Corrosion Sci. 171 (2020) 108722, https://doi.org/10.1016/j.corsci.2020.108722.
[40] M. Wiesener, K. Peters, A. Taube, A. Keller, K.P. Hoyer, T. Niendorf, et al., Corrosion properties of bioresorbable FeMn-Ag alloys prepared by selective laser melting, Mater. Corros. 68 (2017) 1028–1036, https://doi.org/10.1002/maco.201709478.
[41] D. Mei, S.V. Lamaka, J. Gonzalez, F. Feyerabend, R. Willumeit-Römer, M. L. Zheludkevich, The role of individual components of simulated body fluid on the corrosion behavior of commercially pure Mg, Corrosion Sci. 147 (2019) 81–93, https://doi.org/10.1016/j.corsci.2018.11.011.
[42] D. Mei, S.V. Lamaka, C. Feiler, M.L. Zheludkevich, The effect of small-molecule bio-relevant organic components at low concentration on the corrosion of commercially pure Mg and Mg-0.8Ca alloy: an overall perspective, Corrosion Sci. 153 (2019) 258–271, https://doi.org/10.1016/j.corsci.2019.03.039.
[43] C. Wang, C. Tonna, D. Mei, J. Buhagiar, M.L. Zheludkevich, S.V. Lamaka, Biodegradation behaviour of Fe-based alloys in Hanks' Balanced Salt Solutions: Part II. The evolution of local pH and dissolved oxygen concentration at metal interface, Bioact. Mater. (2021) (in press).
[44] S.V. Lamaka, R. Souto, M. Ferreira, In-situ visualization of local corrosion by scanning ion-selective electrode technique (SIET) 3 (2010) 2162–2173.
[45] M.G. Taryba, M.F. Montemor, S.V. Lamaka, Quasi-simultaneous mapping of local current density, pH and dissolved O2, Electroanalysis 27 (2015) 2725–2730, https://doi.org/10.1002/elan.201500286.
[46] M.G. Taryba, K. Van den Bergh, J. De Strycker, O. Dolgikh, J. Deconinck, S. V. Lamaka, Novel use of a micro-optode in overcoming the negative influence of the amperometric micro-probe on localized corrosion measurements, Corrosion Sci. 95 (2015) 1–5, https://doi.org/10.1016/j.corsci.2015.02.037.
[47] S. Lampman, Compressibility and compactibility of metal powders, in: P. Samal, J. Newkirk (Eds.), Powder Metall., vol. 7, ASM International, 2015.
[48] A. Šalak, M. Selecká, Thermodynamic conditions for the Mn–O system in sintering of manganese steels, in: A. Šalak, M. Selecká (Eds.), Manganese in Powder Metallurgy Steels, Cambridge International Science Publishing Ltd., Cambridge, 2012, pp. 5–21.
[49] C.H. Hsu, F. Mansfeld, Technical note: concerning the conversion of the constant phase element parameter Y0 into a capacitance, Corrosion 57 (2001) 747–748, https://doi.org/10.5006/1.3280607.
[50] P. Sharma, P.M. Pandey, Corrosion behaviour of the porous iron scaffold in simulated body fluid for biodegradable implant application, Mater. Sci. Eng. C Biomimetic Supramol. Syst. 99 (2019).
[51] S.J. Cooper, A. Bertei, D.P. Finegan, N.P. Brandon, Simulated impedance of diffusion in porous media, Electrochim. Acta 251 (2017) 681–689.
[52] J. Huang, Diffusion impedance of electroactive materials, electrolytic solutions and porous electrodes: warburg impedance and beyond, Electrochim. Acta 281 (2018) 170–188.
[53] M. Dehestani, K. Trumble, H. Wang, H. Wang, L. Stanciu, Effects of Microstructure and Heat Treatment on Mechanical Properties and Corrosion Behavior of Powder Metallurgy Derived Fe–30Mn Alloy, 2017.
[54] R.-Y. Liu, R.-G. He, L.-Q. Xu, S.-F. Guo, Design of Fe–Mn–Ag alloys as potential candidates for biodegradable metals, Acta Metall. Sin.-Engl. 31 (2018) 584–590, https://doi.org/10.1007/s40195-018-0702-z.
[55] M.S. Dargusch, J. Venezuela, A. Dehghan-Manshadi, S. Johnston, N. Yang, K. Mardon, et al., In vivo evaluation of bioabsorbable Fe-35Mn-1Ag: first reports on in vivo hydrogen gas evolution in Fe-based implants, Adv. Healthc. Mater. 2000667 (2020) 1–15.
[56] Astm G1 - 032017e1, *Standard Practice For Preparing, Cleaning*, and Evaluating Corrosion Test Specimens, West Conshohocken, PA, 2017.
[57] Chemical equilibrium diagrams, Available: https://www.kth.se/che/medusa/.
[58] R. Orinakova, A. Orinak, M. Giretova, L. Medvecky, M. Kupkova, M. Hrubovcakova, et al., A study of cytocompatibility and degradation of iron-based biodegradable materials, J. Biomater. Appl. 30 (2016) 1060–1070, https://doi.org/10.1177/0885328215615459.
[59] Z. Xu, M.A. Hodgson, P. Cao, Effect of immersion in simulated body fluid on the mechanical properties and biocompatibility of sintered Fe-Mn-based alloys, Metals 6 (2016), https://doi.org/10.3390/met6120309.
[60] F.L. Nie, Y.F. Zheng, S.C. Wei, C. Hu, G. Yang, In vitro corrosion, cytotoxicity and hemocompatibility of bulk nanocrystalline pure iron, Biomed. Mater. 5 (2010), 065015, https://doi.org/10.1088/1748-6041/5/6/065015.
[61] P. Sharma, K.G. Jain, P.M. Pandey, S. Mohanty, In vitro degradation behaviour, cytocompatibility and hemocompatibility of topologically ordered porous iron scaffold prepared using 3D printing and pressureless microwave sintering, Mater. Sci. Eng. C 106 (2020) 110247, https://doi.org/10.1016/j.msec.2019.110247.
[62] J. Hu, S.-a. Cao, J. Xie, EIS study on the corrosion behavior of rusted carbon steel in 3% NaCl solution, Anti-Corros. Methods Mater. (2013) 60, https://doi.org/10.1108/00035591311308074.
[63] R. Gorejová, L. Haverová, R. Oriňaková, A. Oriňak, M. Oriňak, Recent advancements in Fe-based biodegradable materials for bone repair, J. Mater. Sci. 54 (2018) 1913–1947, https://doi.org/10.1007/s10853-018-3011-z.
[64] C. Wang, D. Mei, G. Wiese, L. Wang, M. Deng, S.V. Lamaka, et al., High rate oxygen reduction reaction during corrosion of ultra-high-purity magnesium (accepted), NPJ Mater. Degrad. (2020).